

The *SWIFT* AGN and Cluster Survey I: Number Counts of AGN and Galaxy Clusters

Xinyu Dai¹, Rhiannon D. Griffin¹, Christopher S. Kochanek², Jenna M. Nugent¹, Joel N. Bregman³

ABSTRACT

The *Swift* AGN and Cluster Survey (SACS) uses 125 deg² of *Swift* XRT serendipitous fields with variable depths surrounding γ -ray bursts to provide a medium depth (4×10^{-15} erg cm⁻² s⁻¹) and area survey filling the gap between deep, narrow *Chandra/XMM-Newton* surveys and wide, shallow *ROSAT* surveys. Here we present a catalog of 22,563 point sources and 442 extended sources and examine the number counts of the AGN and galaxy cluster populations. SACS provides excellent constraints on the AGN number counts at the bright end with negligible uncertainties due to cosmic variance, and these constraints are consistent with previous measurements. We use *WISE* mid-infrared (MIR) colors to classify the sources. For AGN we can roughly separate the point sources into MIR-red and MIR-blue AGN, finding roughly equal numbers of each type in the soft X-ray band (0.5–2 keV), but fewer MIR-blue sources in the hard X-ray band (2–8 keV). The cluster number counts, with 5% uncertainties from cosmic variance, are also consistent with previous surveys but span a much larger continuous flux range. Deep optical or IR follow-up observations of this cluster sample will significantly increase the number of higher redshift ($z > 0.5$) X-ray-selected clusters.

Subject headings: catalogs — surveys — X-rays: galaxies: clusters — galaxies: active — galaxies: clusters: general

¹Homer L. Dodge Department of Physics and Astronomy, University of Oklahoma, Norman, OK, 73019, xdai@ou.edu

²Department of Astronomy and the Center for Cosmology and Astroparticle Physics, Ohio State University, Columbus, OH 43210

³Department of Astronomy, University of Michigan, Ann Arbor, MI 48109

1. Introduction

X-ray (0.2–10 keV) surveys are fundamental tools to comprehensively study populations of X-ray sources including active galactic nuclei (AGN), clusters and groups of galaxies, starburst galaxies, normal galaxies and their evolution. The most recent X-ray survey of the whole sky is the *ROSAT* All Sky Survey (RASS, Voges et al. 1999) with a flux limit of $3 \times 10^{-13} \text{erg cm}^{-2} \text{s}^{-1}$ in the 0.1–2.4 keV band. Surveys with *Chandra* and *XMM-Newton* probe far fainter fluxes over much smaller areas, and at this point more than 20 *Chandra* and *XMM-Newton* surveys have been carried out with different combinations of survey area and depth ranging from the small *Chandra* deep fields (Brandt et al. 2001; Xue et al. 2011) to the wider area XBöotes (Murray et al. 2005) and XMM-LSS (Pierre et al. 2004) surveys (see the review by Brandt & Hasinger 2005, Figure 1).

Since even the largest *Chandra* and *XMM-Newton* survey areas are $\sim 10 \text{ deg}^2$, there is a need for intermediate depth, wider area surveys to fill the gap between these small, deep surveys and the wider area, shallow surveys based on RASS. Since (to zeroth order) survey volume scales as $V \propto \Omega f_{lim}^{-3/2}$ with survey area Ω and flux limit f_{lim} , surveys of very different depths can have the same overall volumes. They will differ, however, in the redshifts they best probe. RASS cluster surveys like the *ROSAT* Brightest Cluster Sample (BCS, Ebeling et al. 2000) and the *ROSAT*-ESO Flux Limited X-ray survey (REFLEX, Bohringer et al. 2004) are well-designed for studies of clusters in the low redshift universe, while deep fields are well-designed for studies of lower luminosity, high redshift AGN. Shallow surveys, however, lack the depth to produce large samples at intermediate redshifts to probe the evolution of clusters, and deep surveys tend to have their survey volumes at redshifts where clusters are rare. Similarly, shallow (deep) surveys characterize the bright (faint) AGN populations well, but both do poorly for the intermediate luminosity populations and redshifts needed to link the two extremes. Pencil beam surveys, particularly at $z < 1$, also are strongly affected by cosmic variance. Filling this gap requires surveying 100s of square degrees to intermediate depths.

Most existing medium-deep, wide area X-ray surveys are serendipitous surveys built from jointly analyzing large numbers of archival pointed observations originally obtained for other purposes. This includes *ROSAT* pointed serendipitous surveys such as RIXOS (Castander et al. 1995), RDCS (Rosati et al. 1995; 1998), SHARC (Collins et al. 1997; Burke et al. 1997), WARPS (Scharf et al. 1997; Jones et al. 1998; Perlman et al. 2002), 160 deg^2 (Vikhlinin et al. 1998), its extension 400 deg^2 (Burenin et al. 2007), ROXS (Donahue et al. 2001), and BMW (Campana et al. 1999). Similarly, the ChaMP Survey (Kim et al. 2004) pursues the same goals using archival *Chandra* data. There are exceptions, like the RASS NEP (Henry et al. 2001) survey which was based on the repeatedly scanned North Ecliptic

Pole regions. The *ROSAT* surveys still provide the best constraints on the bright end of the cluster X-ray luminosity function and the high redshift cluster mass function (Rosati et al. 2002; Vikhlinin et al. 2009) due to their large survey area. The *XMM-Newton* and *Chandra* serendipitous surveys are still on going (e.g., Watson et al. 2009; Lloyd-Davies et al. 2011; Fassbender et al. 2011; Clerc et al. 2012). These surveys cover sky areas of 10–400 deg², and have flux limits from 5×10^{-14} to 10^{-15} erg cm⁻² s⁻¹. One disadvantage of most of these serendipitous surveys based on pointed archival data is that the selection effects are difficult to model without a complete understanding of why the original targets were selected. Figure 1 shows where some of these surveys lie in the space of area and depth.

In this paper, we present a serendipitous medium-deep, wide-field soft X-ray survey using *Swift* (Gehrels et al. 2004; Burrows et al. 2005; Morette et al. 2005) observations of γ -ray bursts (GRBs). From its launch in November 2004 through July 2013, *Swift* has observed 784 GRBs at a rate of ~ 92 bursts per year. The X-Ray Telescope (XRT) on board *Swift* is sensitive in the energy range from 0.2–10 keV and has a field of view of 23.4×23.4 arcmin². These GRB fields are randomly distributed on the sky (Figure 2) and are essentially uncorrelated with other X-ray source populations. Thus, the XRT observations of GRB fields form an excellent soft X-ray serendipitous survey covering a total sky area of ~ 125 deg² with variable depths and a median flux limit of 4×10^{-15} erg cm⁻² s⁻¹. Figure 1 shows the relative depth and sky coverage of these *Swift* serendipitous fields compared to other surveys. This unique combination of the survey area, survey depth and “randomness” enables it to fill in the gap between deep, pencil beam surveys such as the *Chandra* Deep Fields and the shallow, wide area *ROSAT* surveys. Thus it can be used to make independent and complementary measurements of the number counts and luminosity functions of X-ray sources, principally AGN and galaxy clusters. This will in turn strengthen our understanding of the evolution of X-ray sources and the underlying cosmology. Several other groups are also independently working with this data, focusing on bright clusters (Tundo et al. 2012; Liu et al. 2013), point sources in deep XRT fields (Puccetti et al. 2011), and on the overall source catalog of all XRT observations (D’Elia et al. 2013; Evans et al. 2014).

In §2 we describe our field selection, the reduction of the XRT data and the detection of sources. In §3 we classify the sources based on the X-ray angular extent and matches to the Wide-field Infrared Survey Explorer (*WISE*, Wright et al. 2010) survey catalogs. In §4 we compare our catalogs with other independent *Swift* XRT catalogs. In §5 we compare the source number counts to existing estimates from both shallower and deeper surveys, and we discuss the results in §6. We assume cosmological parameters of $\Omega_M = 0.27$, $\Omega_\Lambda = 0.73$, $\sigma_8 = 0.81$, and $H_0 = 70$ km s⁻¹ Mpc⁻¹ throughout the paper.

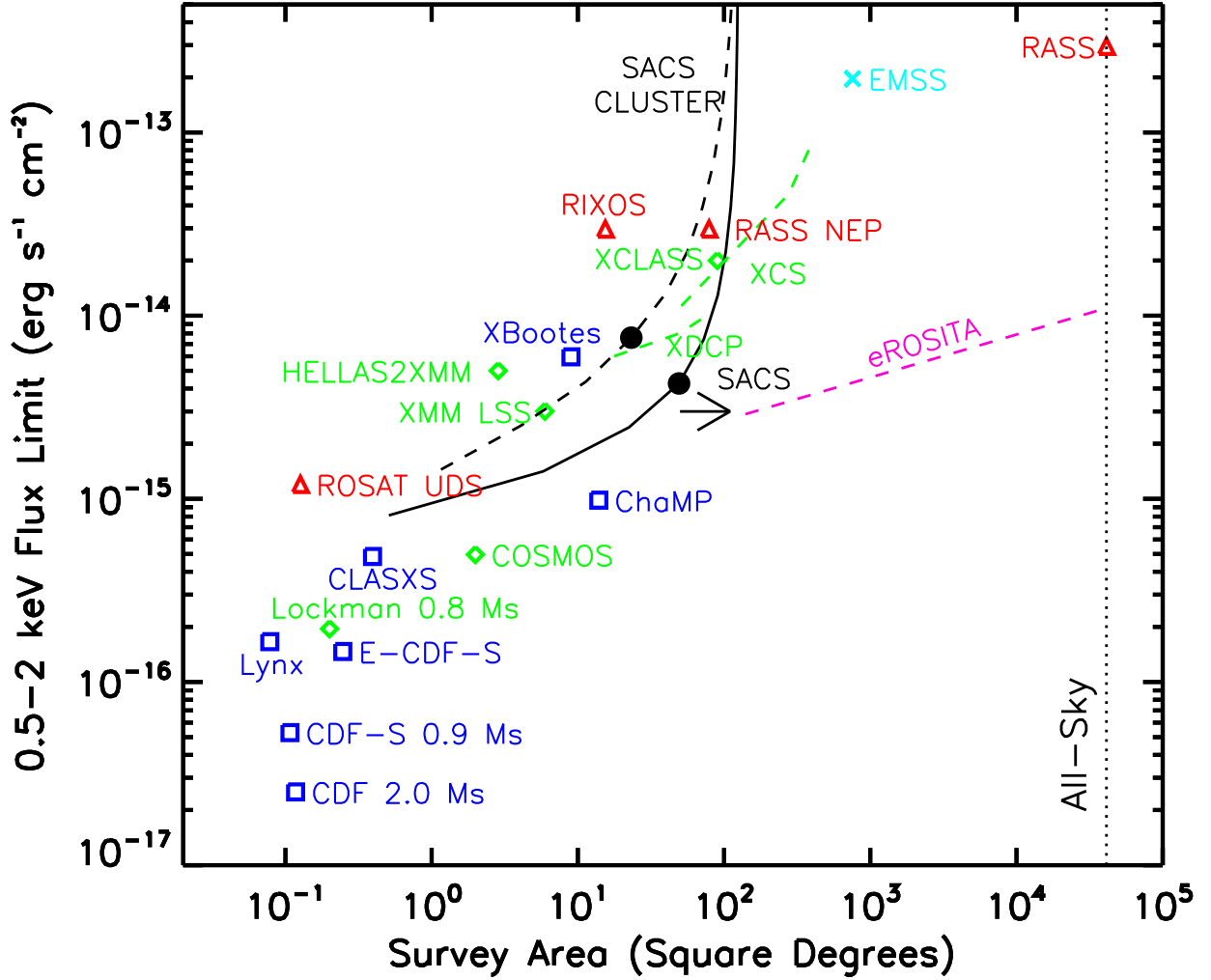


Fig. 1.— Comparison of the flux limit and survey area of the *Swift* AGN and Cluster Survey (SACS) through July 2013 to other soft X-ray surveys from Brandt & Hasinger (2005), adding recent *XMM-Newton* medium deep surveys, and the future *eROSITA* surveys. SACS (solid and dashed lines for point and extended sources) is substantially wider or deeper than many similar existing surveys, and the arrow shows that SACS is approaching the *eROSITA* deep survey as *Swift* continues to accumulate data. The solid circles indicate the typical SACS field, 49 square degrees and 4.3×10^{-15} erg cm $^{-2}$ s $^{-1}$ for point sources and 23 square degrees and 7.6×10^{-15} erg cm $^{-2}$ s $^{-1}$ for extended sources, in the 0.2–5 keV band.

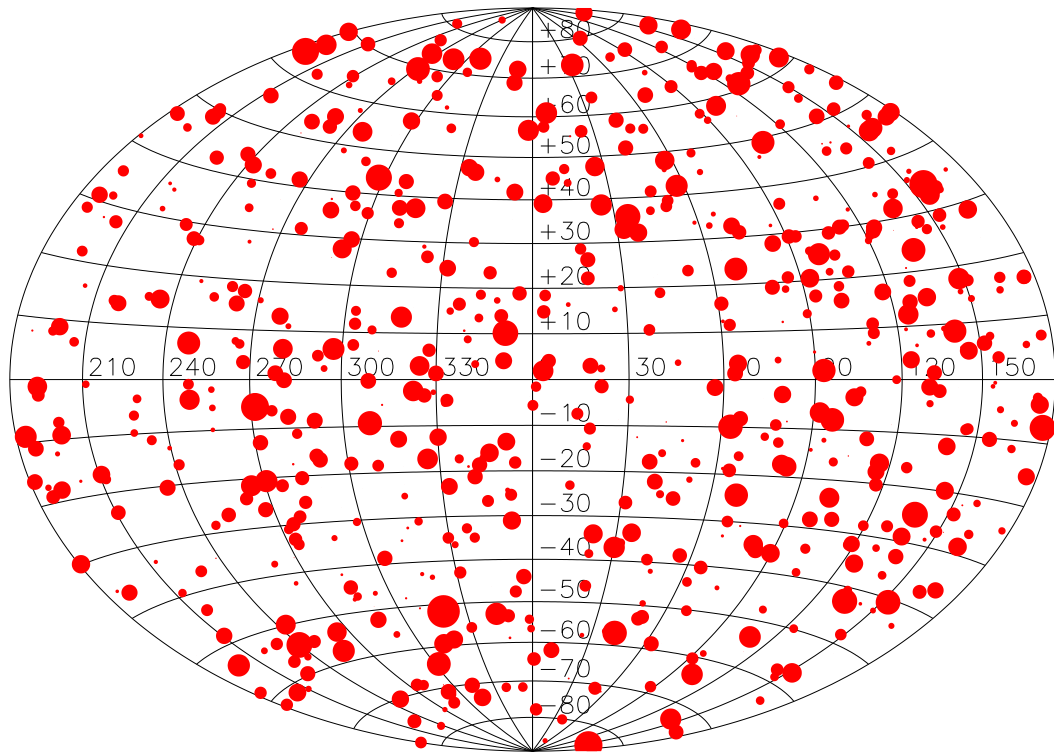


Fig. 2.— Distribution of *Swift*-XRT GRB observations in Galactic coordinates. Larger point sizes indicate longer exposure times.

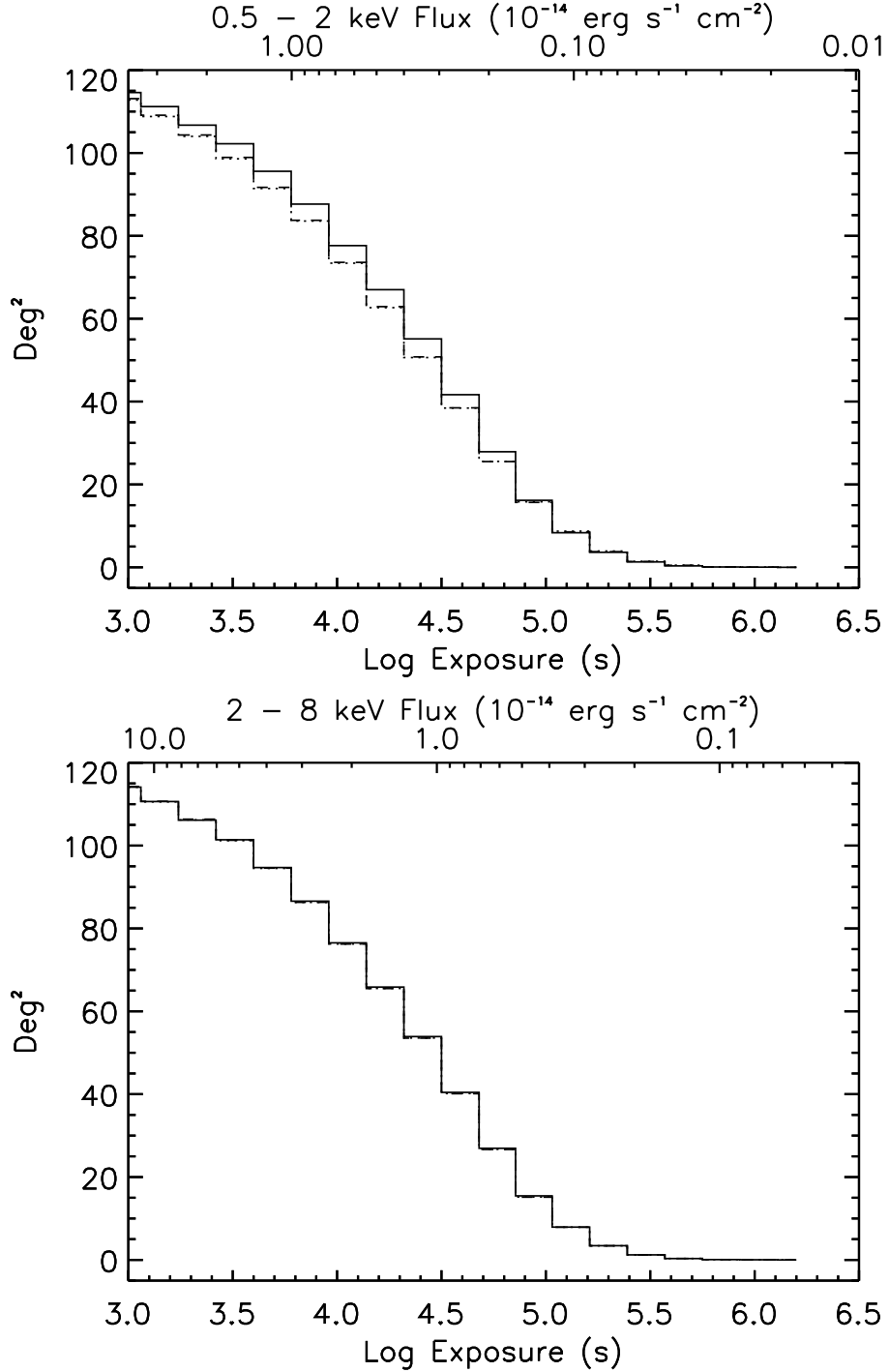


Fig. 3.— Cumulative distribution of survey area as a function of the equivalent on-axis exposure time for the soft (0.5–2 keV, upper panel) and hard (2–10 keV, bottom panel) X-ray bands. The dotted and dashed lines show the effect of smoothing the exposure maps over 6 and 10 XRT pixels, the typical sizes of point and extended sources, and with a nominal Galactic N_{H} of $5 \times 10^{20} \text{cm}^{-2}$. In the hard band, the curves are almost completely overlapping. The upper X-axis shows the corresponding flux limits based on the median background rates of the fields and a typical Galactic N_{H} of $5 \times 10^{20} \text{cm}^{-2}$.

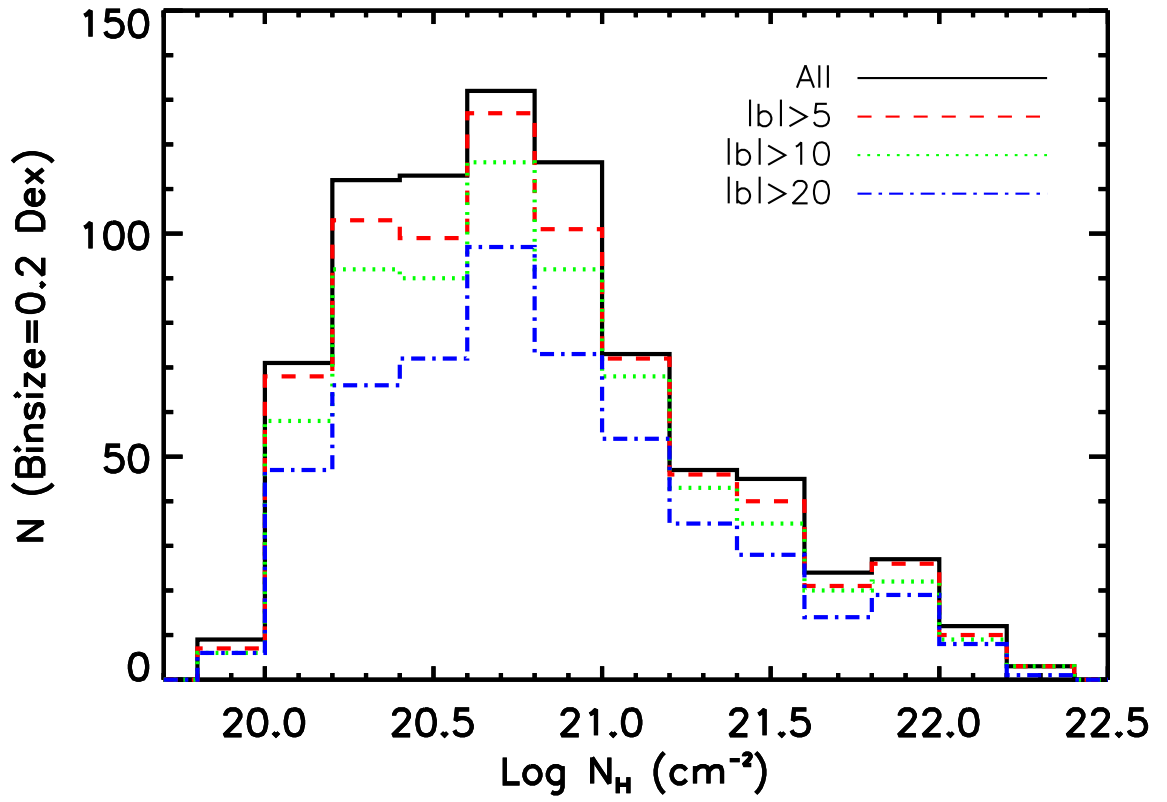


Fig. 4.— Galactic N_{H} column density for all of the *Swift* fields (black solid line), and those with Galactic latitudes of $|b| \geq 5$ (red dashed line), $|b| \geq 10$ (green dotted line), and $|b| \geq 20$ (blue dot-dashed line), respectively.

2. Data Reduction and Source Detections

The *Swift* XRT observations of GRB fields were downloaded from the HEASARC website¹. This includes all XRT observations before 2013–07–27 with target names containing “GRB”, but excluding special targets with names such as “Non-GRB”. We lose the very small fraction ($< 1\%$) of XRT GRB observations without “GRB” in their target names (usually instead having target names starting with “Swift J”). We reprocessed the data using the HEASoft tool `xrtpipeline` (version 0.12.6) and *Swift* CALDB version XRT20130313. We generated the corresponding exposure maps using `xrtexpomap` (version 0.2.7). XRT follow-up observations of GRBs are typically a monitoring sequence to measure the decay of the X-ray light emission, so we merged all the reprocessed event files and exposure maps for each GRB field into a single event file and a single exposure map in order to increase the signal-to-noise (S/N) ratio for detecting serendipitous sources. We then created images in the total (0.2–10 keV), soft (0.5–2 keV), and hard (2–10 keV) bands from the merged event files. Figure 3 shows the cumulative area of the final field sample as a function of the equivalent on-axis exposure time and Figure 4 shows the distribution of the fields in Galactic N_{H} column density based on Dickey & Lockman (1990). Since the N_{H} distribution for XRT fields with low Galactic latitudes, $|b| < 5^\circ$, is similar to those from high Galactic latitudes, we included all these XRT fields in our analysis.

We used a wavelet-based algorithm (`wavdetect`, Freeman et al. 2002) in CIAO to identify sources, an algorithm which is widely used in the X-ray community to detect sources in *Chandra* and *ROSAT* images. Since one of our goals is to separate point AGN from extended clusters, the angular structure of the *Swift*/XRT point spread function (PSF) has several advantages. First, its dependence on off-axis angle and energy are well measured by the *Swift* team (Moretti et al. 2005) and released as a part of the calibration files. Second, the on-axis half power diameter (HPD) of 17–18” is reasonably well-suited for cluster identification. More importantly it is roughly constant over the full field of view, unlike *Chandra* and *ROSAT* (Weisskopf et al. 2002; Hasinger et al. 1994) where they are very strong functions of off-axis angles. For example, at 1.5 keV, the on-axis HPD is 18”3, slowly declining to 15”1 for a 10’ off-axis angle. For *Chandra* and *ROSAT*, the HPDs of 12”4 and 21” at 10’ off-axis are much larger than the on-axis HPDs of 0”84 and 14”. The PSF of *XMM-Newton* has smaller differences, but still increases from 15” (13”) on-axis to 19” (21”) at 10’ off-axis for the PN (MOS) cameras (Jansen et al. 2001). The relatively uniform PSF also significantly reduces systematic uncertainties when assessing the significance of source detections and their angular sizes. We used `wavdetect` to detect sources in the total, soft, and hard images

¹The HEASARC website is at <http://heasarc.gsfc.nasa.gov>.

independently using a false positive threshold of 10^{-6} . We further evaluated the significance of the detections using the net source and background counts provided by `wavdetect` and Equation A11 of Weisskopf et al. (2007) for Poisson statistics,

$$P = \Gamma(N_{Total}, N_{Bkg}) / \Gamma(N_{Total}), \quad (1)$$

where $N_{Total} = N_{Src, Net} + N_{Bkg}$, and rejected sources with significance less than 0.997 from the final catalog. These final catalogs are presented in Tables 1–4, where we have used the results of the next section to separate them into candidate AGN and galaxy clusters. Tables 1 to 3 present the 22,563, 17,748, and 10,060 total, soft, and hard band AGN candidates and Table 4 presents the 442 cluster candidates. We corrected the fluxes for the finite aperture used in the measurements. For point sources we simply use the PSF, while for the extended sources we assumed a $\beta = 0.6$, $R_c = 0.1$ Mpc β model (e.g., Sanderson et al. 2003) at the typical cluster redshift of $z = 0.5$ and estimated the total flux inside 2 Mpc. This typically increased the fluxes by a factor of 1.3. Similarly, we assume a $T = 5$ keV, $Z = 0.4Z_\odot$ plasma spectrum at $z = 0.5$ to correct their fluxes for Galactic absorption. In the number count calculations (Section 5), we set the Galactic absorption as $N_H = 5 \times 10^{20} \text{cm}^{-2}$ for all sources; however, we adopted the Dickey & Lockman (1990) Galactic absorption values when reporting the fluxes in Tables 1–4.

3. Classification of the X-ray Sources

The vast majority of our sources will be extragalactic sources, AGN, GRBs and galaxy clusters, since only a small fraction of XRT observations are in the Galactic plane and Galactic X-ray sources are typically fainter. Our matching analysis with *WISE* sources also suggests that there are few Galactic sources in our catalogs (Section 3.2). In this section we discuss the classification of the sources using their X-ray angular extent and their properties, where detected, in the all-sky *WISE* catalogs. We first matched our sources to the known positions of the GRB X-ray afterglows using the most recent catalogs from the UK XRT team². We used a matching radius of $24''$ even though the *Swift* XRT HPD is about $18''$. The XRT position of GRBs can be measured much more accurately because of the large number of photons detected in GRBs. However, for bright GRBs a large fraction of photons located near the center of the GRB image can be rejected during the data reduction process because of strong pile-up effects. These sources are then found by `wavdetect` as a source pair slightly offset from the true position but always within $24''$ of each other. Since the

²Available at http://www.swift.ac.uk/xrt_positions/.

GRB science is not the main focus of this paper and to avoid its strong contamination to other sources, we remove all sources within $24''$ of the GRB positions. The next step is to use the angular source extent to distinguish between AGN and galaxy clusters.

3.1. Extended Source Analysis

All galaxy clusters are extended X-ray sources given an ideal telescope. Cluster surface brightness profiles are well-modeled by the so-called β profile, $S \propto (1 + (R/R_c)^2)^{-3\beta+1/2}$ (e.g., Xu et al. 2001; Sanderson et al. 2003; Dai et al. 2007, 2010). The core radius R_c and power law index β depend on cluster mass (Xu et al. 2001; Sanderson et al. 2003; Dai et al. 2007, 2010), and values of (0.2 Mpc, 0.67), (0.1 Mpc, 0.6) and (0.05 Mpc, 0.5) are typical for clusters with masses of 10^{15} , 2×10^{14} and $5 \times 10^{13} M_\odot$ (e.g., Neumann & Arnaud 1999; Xu et al. 2001; Sanderson et al. 2003; Osmond & Ponman 2004; Dai et al. 2010). The *Swift* XRT PSF has a moderate HPD ($15\text{--}18''$) and is also well-modeled by a β profile with $\beta \simeq 0.67$ and $R_c \simeq 2.3$ XRT pixels with variations across the field of view that are well understood (Moretti et al. 2005).³ The observed profile of a cluster is then the convolution of the appropriate β model with the PSF. For simplicity, we will simply view this as a β model with different parameters.

We used only the soft band images to study the source surface brightness profiles because of their higher contrasts for cluster emission, and used an iterative procedure in this analysis. From the merged soft X-ray image of each field, we extracted background-subtracted surface brightness profiles of each source out to the radius r_b , where the surface brightness equals half the background level and the initial guesses were set to two times the source radii given by `wavdetect`. We then fit these surface brightness profiles with β models, with $\beta = 0.67$ fixed for all sources. This is optimal for the vast majority of point sources and massive clusters. Sources were analyzed in the order of their brightness, and when we analyzed sources we included the flux contributions from other nearby sources. We started with the brightest source, fixing the parameters of all other sources in the model when fitting each individual source, and sequentially moved down to the faintest source. We then iterated this procedure until the model parameters (R_c and total flux) for all the sources converge.

We analyzed simulated sources to estimate the detection thresholds for extended sources by adding 1000 simulated clusters to real images and then using our detection algorithm to recover the extended sources and their properties. Similarly, we added the same number of

³ In Moretti et al. (2005), this is described as being a King profile, $(1 + (R/R_c)^2)^{-\alpha}$, which is just a β model with $\alpha = 3\beta - 1/2$.

simulated point sources and recovered their properties. Here, we used the R_c and β pair of (0.1 Mpc, 0.6) for clusters with total masses of $\sim 2 \times 10^{14} M_\odot$, which correspond to our typical cluster detection limit. Figure 6 shows an example of the probability of distinguishing extended and point sources as a function of the net number of photons for images with a typical exposure time of 60 ks. For the significance of the difference to exceed 3σ , it requires 17–30 net photons for clusters from $z = 0.6$ – 1.4 , which correspond to fluxes of 0.6 – 1.1×10^{-14} erg cm $^{-2}$ s $^{-1}$ in the 0.5–2 keV band for a typical XRT field. Higher numbers of photons are needed for higher redshift clusters as the angular sizes of the clusters become smaller. More massive clusters have larger core sizes (e.g., $R_c = 0.2$ Mpc), which are easier to separate from point sources. Using the same R_c and β pair (0.1 Mpc, 0.6), we carried out these simulations for the range of backgrounds encompassing the shallowest and deepest observations and these can be used to model the completeness of the cluster sample (Table 5).

Figures 7 and 8 show the distribution of sizes (R_c) for the sources detected in the XRT images as a function of the off-axis angle and the signal-to-noise ratio of the detection. There is a dominant band of point sources with $R_c \simeq 2.5$ XRT pixels ($6''$), as expected from the PSF models. The mean size of the point sources is essentially independent of the off axis angle, as expected from the uniformity of the PSF, and the scatter in the sizes increases for lower signal-to-noise ratios. To estimate the boundary for selecting extended sources we set an initial boundary that roughly separated the point and extended sources and then calculated the mean and standard deviation of the point source sizes. We then updated the 3σ boundary and iterated this procedure until the estimates converged. This was done as a function of both off-axis angle and signal-to-noise ratio with the results also shown in Figures 7 and 8. We defined the extended source catalog as sources with $S/N \geq 4$ and a minimum net photon count of 20 that are more than 3σ from the mean size of point sources for both their off-axis angle and signal-to-noise ratio. This resulted in 442 cluster candidates.

We matched our cluster catalog with the meta X-ray cluster catalog (Piffaretti et al. 2011) using a match distance of 0.5, and found seven matches. In particular, SWCL J025630.7+000601, J062915.2+460619, J155743.3+353020, J180228.7-523651, J181628.8+691131, J214359.4-563725, and J233616.8-313629 match with MCXC J0256.5+0006, MCXC J0629.1+4606, MCXC J1557.7+3530, MCXC J1802.4-5236, MCXC J1816.5+6911, MCXC J2143.9-5637, and MCXC J2336.2-3136, respectively. We also matched to the ACT and *Planck* SZ cluster catalogs (Marriage et al. 2011; Planck Collaboration et al. 2014) and found that SWCL 025630.7+000601 matches ACTCL J0256.5+0006 within 0.5 and SWCL J084749.4+133142 matches with PSZ1 G213.43+31.78 within 2.9. We also found 22 matches to the optical cluster catalogs (Koester et al. 2007; Hao et al. 2010) in the SDSS footprint, and the details are discussed in Griffin et al. (2015, in preparation). We matched with the independent *Swift* cluster catalog of Tundo et al. (2012) with 72 entries and found 55 matches (see Section 4).

Therefore, the majority of our *Swift* clusters are new discoveries.

3.2. Matching to *WISE*

The only all-sky catalog with a depth well-matched to our survey is the mid-infrared (MIR) *WISE* (Wright et al. 2010) survey, which also automatically includes matches to the shallower *2MASS* survey (Skrutskie et al. 2006). There are significant overlaps with other surveys, particularly SDSS, but nothing else provides uniform coverage. In Griffin et al. (2015) we examine the properties of the lower redshift ($z < 0.5$) cluster candidates in the SDSS regions, but deeper data than SDSS are needed study cluster properties in general. Mid-IR colors are also a powerful and well-understood means of identifying AGN (e.g., Stern et al. 2005) including examinations of AGN selection from *WISE* data (e.g. Assef et al. 2013). X-ray emission and MIR colors do not select identical AGN samples. Like X-rays, MIR selection is fairly insensitive to absorption. However, it does depend on the slope of the MIR spectrum being different from that of a galaxy, which means that the AGN must make a significant contribution to the total MIR luminosity. As a result, MIR selection will not identify very low luminosity AGN. Chung et al. (2014) has an extensive comparison of X-ray and MIR selection methods. We also improve the astrometry of the *Swift*-XRT sources by correcting the pointing accuracy of XRT ($3''$, Burrows et al. 2005) during the *WISE* matching analysis.

We searched for the closest source to the position of each XRT source and to random positions along a circle of radius $120''$ around the XRT position. We kept the closest *WISE* source to both the real and random positions provided the separation was smaller than $20''$. For each GRB field, we calculated the mean ΔRA and ΔDec and variance of these means for real matches, and corrected the X-ray source astrometry if any mean offset is larger than the standard deviation of the mean offsets. The median and maximum RA corrections are $1''.36$ and $5''.01$, and the median and maximum Dec corrections are $1''.31$ and $4''.36$. The top and bottom panels of Figure 9 show the distributions of the match distances for real and random sources after correcting the XRT astrometry and after normalizing the random distribution to match the real distribution on scales of $15\text{--}20''$. For the real sources we see a central core peaking at $\sim 2''$, with a non-zero peak, as expected from a χ^2 distribution. The probability that a match is correct as a function of distance can be roughly estimated as $1 - N_{\text{fake}}/N_{\text{real}}$ and we also show this probability as a function of match distance. The match probabilities are roughly 80%, 86%, and 85% at a distance of $4''.5$, and 53%, 51%, and 56% at a distance of $7''.5$ for the total, soft, and hard bands, respectively. Overall we estimate that 61%, 65%, and 65% of the total, soft and hard band sources have *WISE* counterparts. The fraction is

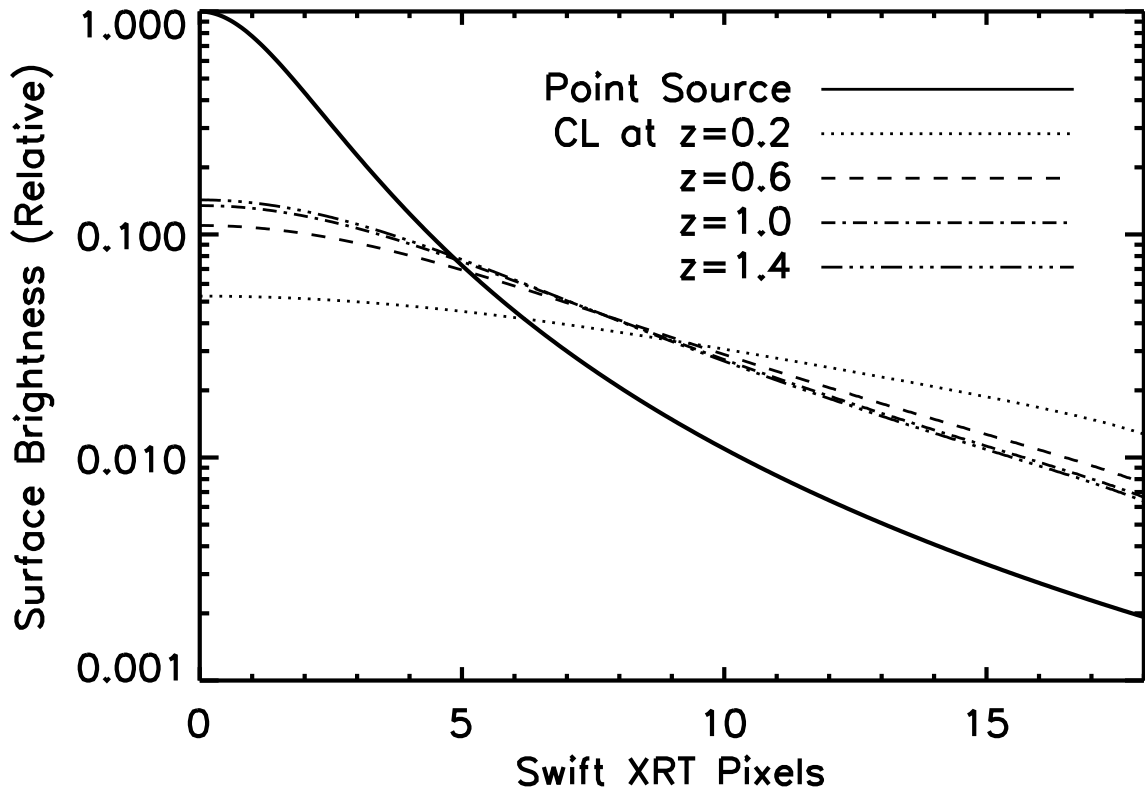


Fig. 5.— Simulated surface brightness profiles for a point source (solid line) and a cluster with the same flux ($R_c = 100$ kpc, $\beta = 0.6$) at redshifts of $z = 0.2, 0.6, 1.0$ and 1.4 convolved with the *Swift*-XRT PSF. Even at redshift $z = 1.4$, clusters are clearly more extended than point sources.

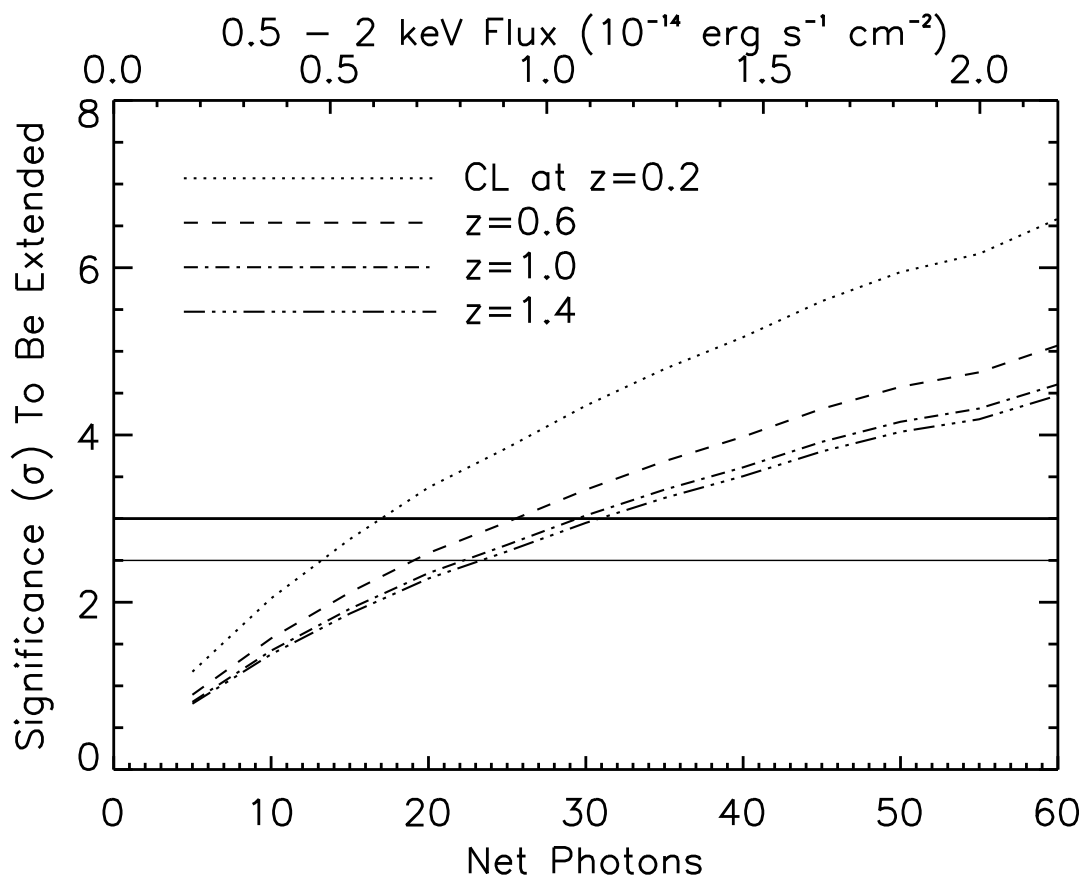


Fig. 6.— Significance with which a cluster ($R_c = 100$ kpc, $\beta = 0.6$) can be detected for redshifts of $z = 0.2, 0.6, 1.0$ and 1.4 as a function of the net number of photons in an image with a typical exposure time of 60 ks. The two horizontal solid lines show the 2.5σ and 3σ significance levels. The upper X-axis shows the corresponding flux.

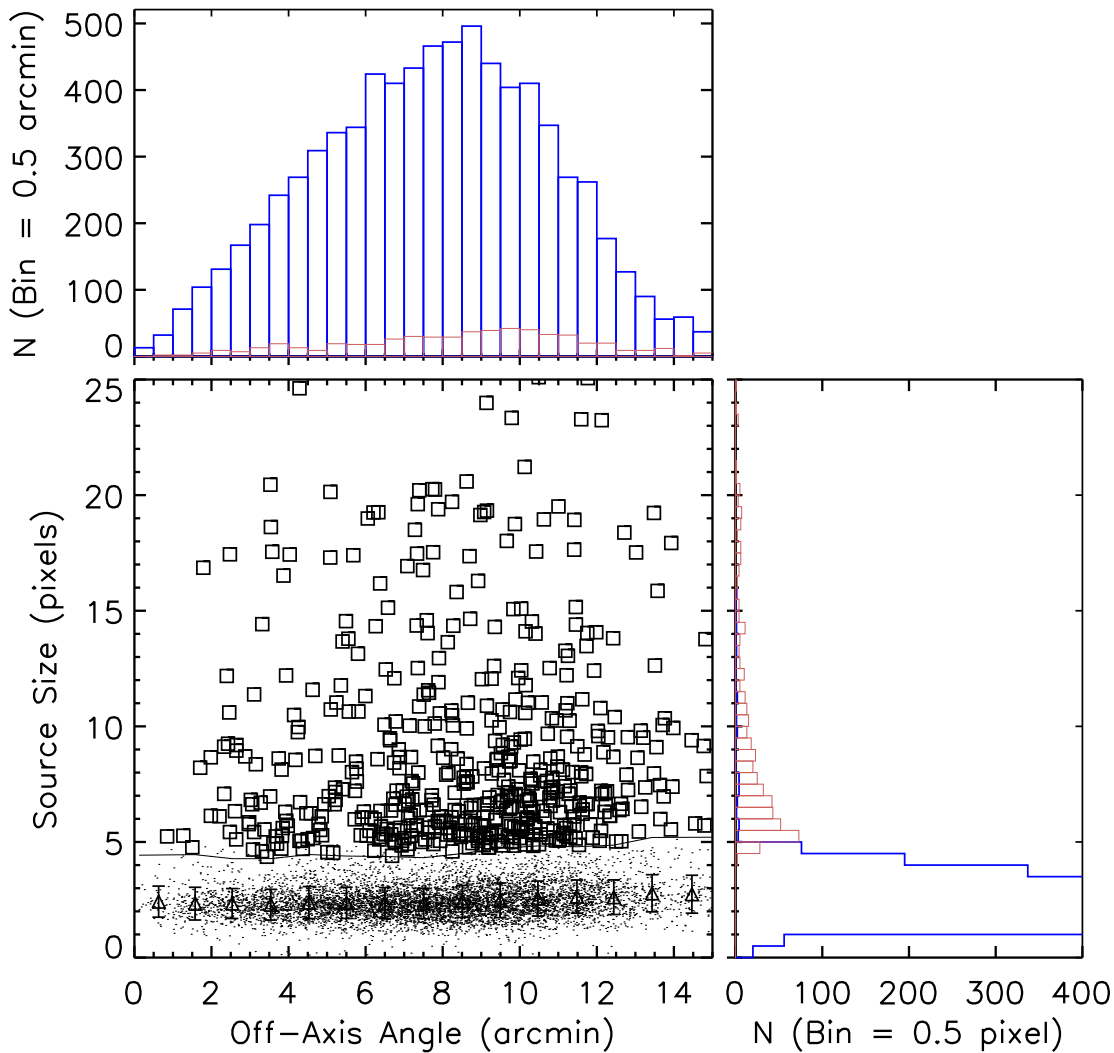


Fig. 7.— The core radius R_c distribution for the 17 thousand 0.5–2 keV sources detected in the *Swift* GRB fields as a function of the source off-axis angle. The triangles with error bars show the mean size of the point sources and the standard deviation about the mean. The line shows the 3σ size cut used to separate point sources (solid line) from extended sources (open squares). The upper and right histograms show the R_c and off-axis angle histograms for point sources (blue) and extended sources (red).

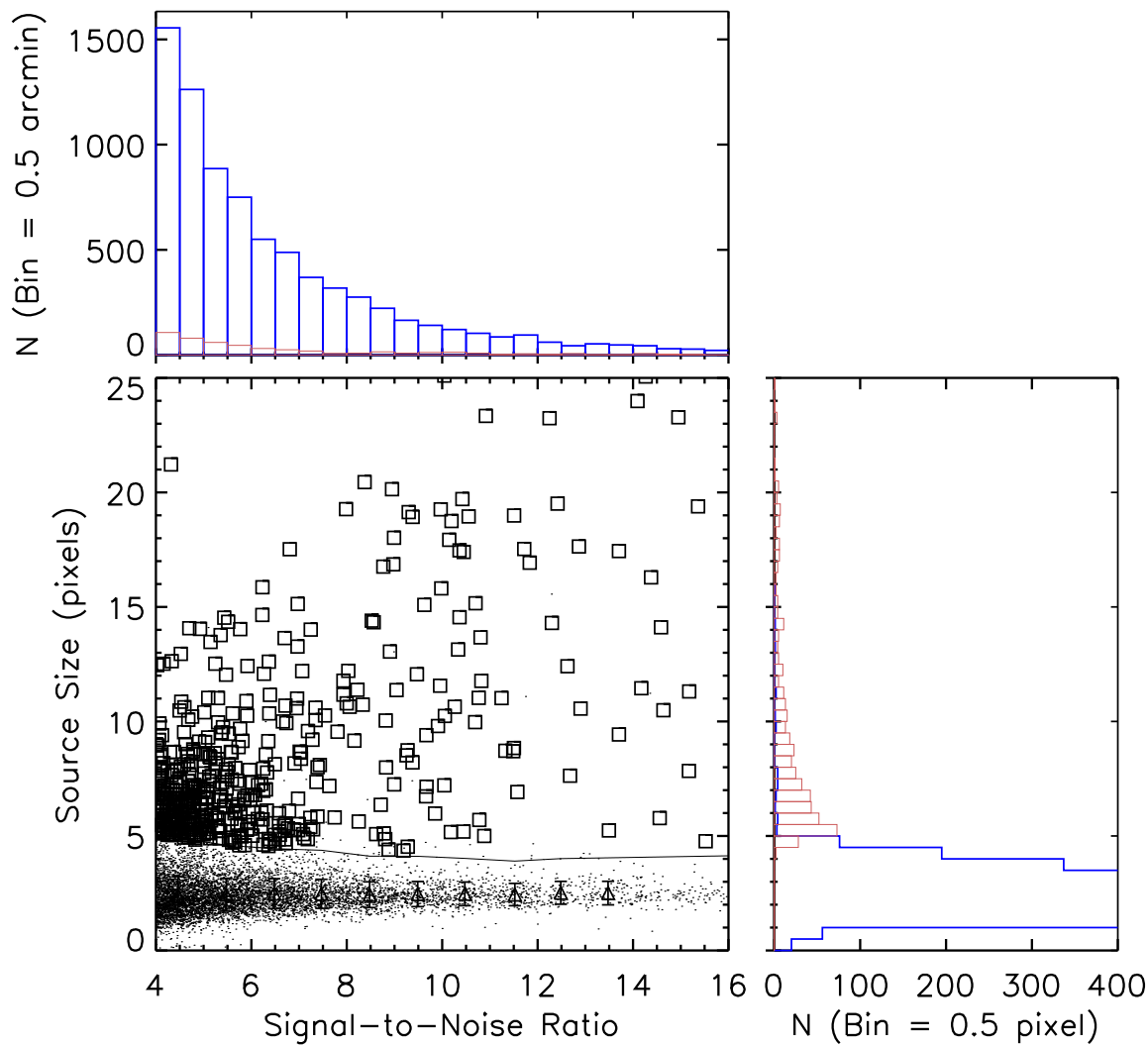


Fig. 8.— The core radius R_c distribution of the 17 thousand sources detected in the *Swift* GRB fields as a function of the S/N. As in Figure 7 the triangles with error bars show the mean size of the point sources and the standard deviation about the mean. The line shows the 3σ size cut used to separate point sources (solid line) from extended sources (open squares). The upper and right histograms show the S/N and R_c histograms for point sources (blue) and extended sources (red).

higher for the hard and soft band catalogs simply because the flux limits will be brighter.

The distribution of matches for the extended sources looks quite different. First, while 12% of the total band AGN sample had no *WISE* source within $20''$, only 6% of the cluster candidates had no source within that distance. Second, while $2/3$ of the AGN candidates had a closest source with a red MIR color ($W1 - W2 > 0.35$ mag), less than $1/2$ of the cluster candidates do so. This *does not* mean that $1/2$ of the cluster candidates are AGN because of the significant noise in the MIR colors at fainter magnitudes (see Assef et al. 2013). Third, the match distance distribution of the sources is broader, as we would expect for extended sources being matched to a local distribution of galaxies. Overall, 72% of the extended sources are probably associated with a *WISE* source.

The *WISE* color magnitude diagram is a useful diagnostic to separate AGN and galaxies. We focus on the deeper W1 ($3.4\mu\text{m}$) and W2 ($4.6\mu\text{m}$). In these Vega magnitudes, stars and early-type galaxies tend to be relatively blue because their MIR spectral energy distributions (SEDs) are dominated by the Rayleigh-Jeans tail of the emission by stars. Quasars have much flatter SEDs and so appear red (e.g., Stern et al. 2005, Assef et al. 2013, Chung et al. 2014). This is true as long as there is significant emission from the quasar accretion disk (at most redshifts, $z \gtrsim 1$, it is not dust emission), and red, MIR selected quasars generally prove to be broad line, Type I AGN (see Kochanek et al. 2012). X-ray sources extend to bluer MIR colors, indicating that the disk emission does not dominate over that of the host (e.g. Gorjian et al. 2008, Chung et al. 2014), and these sources will more likely be Type II AGN. We note that the red and blue MIR colors are opposite to the usual AGN terminology, where MIR-blue AGN correspond to absorbed AGN and MIR-red AGN correspond to less absorbed AGN. For the purposes of the paper we will call sources with *WISE* color, $W1 - W2 > 0.35$ mag, MIR-red AGN, and those with $W1 - W2 \leq 0.35$ mag MIR-blue AGN, although the boundary is imperfect. Moreover, the *WISE* colors are noisy for the typical source we consider because most of the matches are to faint *WISE* sources. This means that the color is only an indicator of the nature of the source. The dependencies of AGN properties on the *WISE* fluxes are discussed extensively in Assef et al. (2013).

Figure 10 shows the color magnitude diagrams for the soft and hard band AGN samples as well as the cluster samples along with the typical colors of galaxies and Type I AGN at various redshifts. Here we use only objects with a match distance smaller than $8''$. As expected, the AGN samples tend to have relatively red MIR colors while the sources matched to clusters have the MIR colors of intermediate redshift galaxies. If we use a two-dimensional Kolmogorov–Smirnov test to compare the distributions of AGN and extended sources, there is a null probability of 4×10^{-26} that the two samples are drawn from the same distribution, further showing that the extended X-ray sources are not significantly contaminated by AGN.

MIR-blue AGN have colors similar to stars as well as galaxies. However, Figure 11 shows that there is no significant Galactic latitude dependence to either the number density of sources or the ratios of the numbers of red and blue MIR sources. This strongly suggests that the level of stellar contamination is small.

4. Comparison with Other *Swift* XRT Catalogs

There are several other *Swift* XRT source catalogs in existence. We can characterize them by the type of sources (point/extended), years of data used (5–7), fields analyzed (GRB or all), and detection method. They are Puccetti et al. (2011, point, 5 year, GRB, `XIMAGE`), D’Elia et al. (2013, point, 7 year, all, `detect`), Evans et al. (2014, point, 7 year, all, similar to the 2XMM catalog of Watson et al. 2009), and Tundo et al. (2012, extended, 6 year, GRB, `wavdetect` plus extended source analysis). Here, we compare them with our catalogs.

We matched the four point source catalogs to each other using a $8''$ match distance and the two extended catalogs using a $30''$ match distance and calculated the match distance distributions. We also calculated the fractional flux differences, $(f_{cat2} - f_{cat1})/f_{cat1}$, of the matching sources in the 0.5–8 keV band for point sources and the 0.5–2 keV band for extended sources. We list the number of matches, the median match distances, the median and standard deviation of the fractional flux differences in Table 6, and show the histograms of the matching distances and fractional flux differences between this paper and Evans et al. (2014) and between this paper and Tundo et al. (2012) in Figures 12 and 13, respectively. In general the source positions are quite consistent between the different catalogs, with median position offsets of $\lesssim 2''$ for point sources and $5''.2$ between the two extended catalogs. The ΔRA and ΔDec distributions are all centered on zero. Since the fractional flux difference distributions have long tails, we calculated the statistical properties of the distributions within the range of -1 to 1 . The fluxes measured from the different catalogs have larger variations, with the standard deviations of the fractional flux differences ranging from 0.15 to 0.39, where the smallest is between the cluster catalog from this paper and Tundo et al. (2012) and the largest is between the point source catalogs of D’Elia et al. (2013) and Evans et al. (2014). The D’Elia et al. (2013) catalog also has the largest median offset in the fractional flux difference when matching with other catalogs. Broadly speaking, our point and cluster catalogs have position and flux measurements consistent with these other analyses. We compare the flux distributions between our sources and those in Evans et al. (2014) and Tundo et al. (2012) for point and extended sources, respectively, in Figure 14. For point sources, Evans et al. (2014) analyzed a much larger amount of *Swift* data and detected a total number of sources 6.7 times our total number. However, our peak flux distribution is fainter than the sample

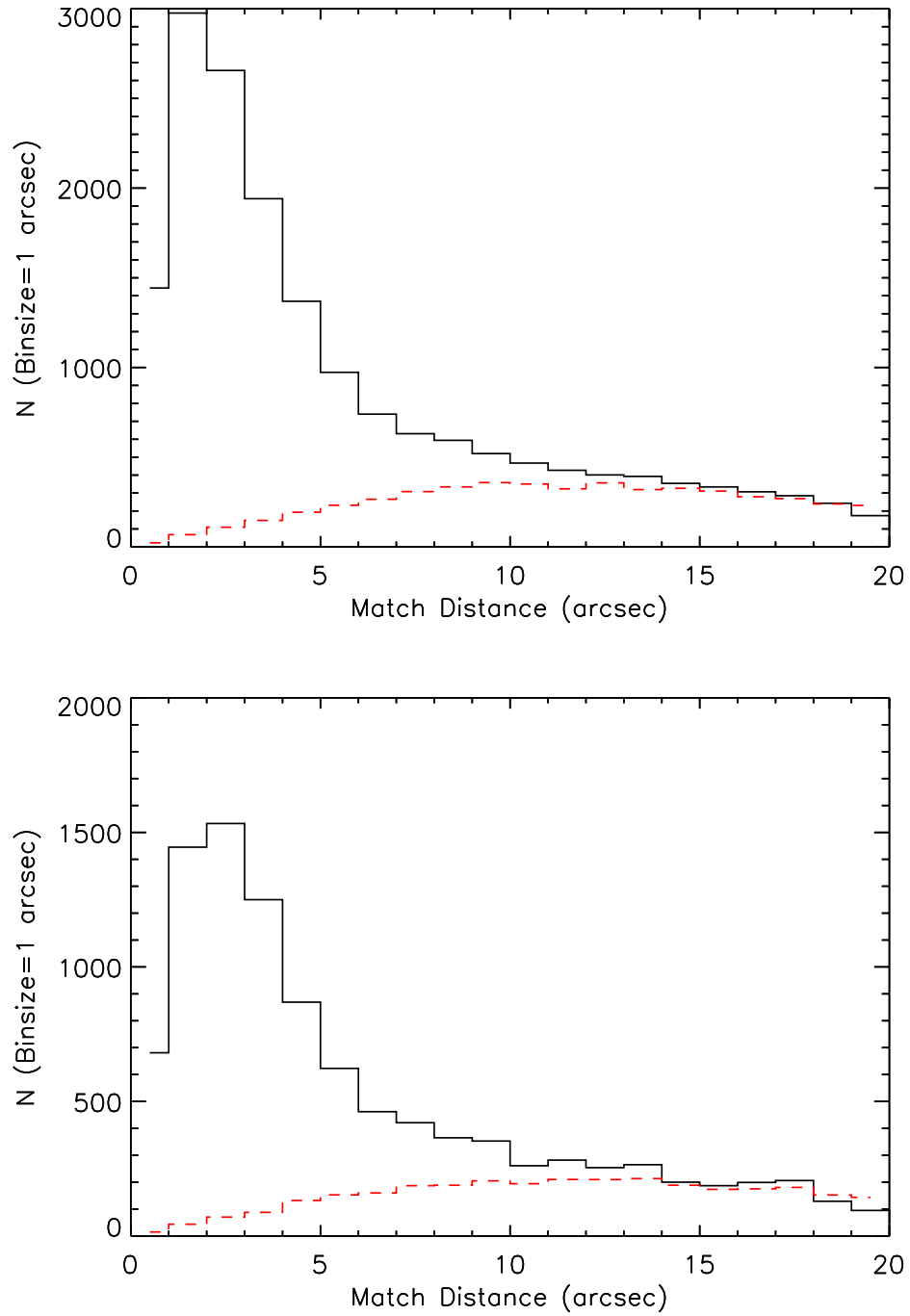


Fig. 9.— Histograms of the distance between the soft (top) and hard (bottom) band *Swift* X-ray source and the closest *WISE* source. The black solid histogram is for the real X-ray sources, while the red dashed line is for nearby random positions.

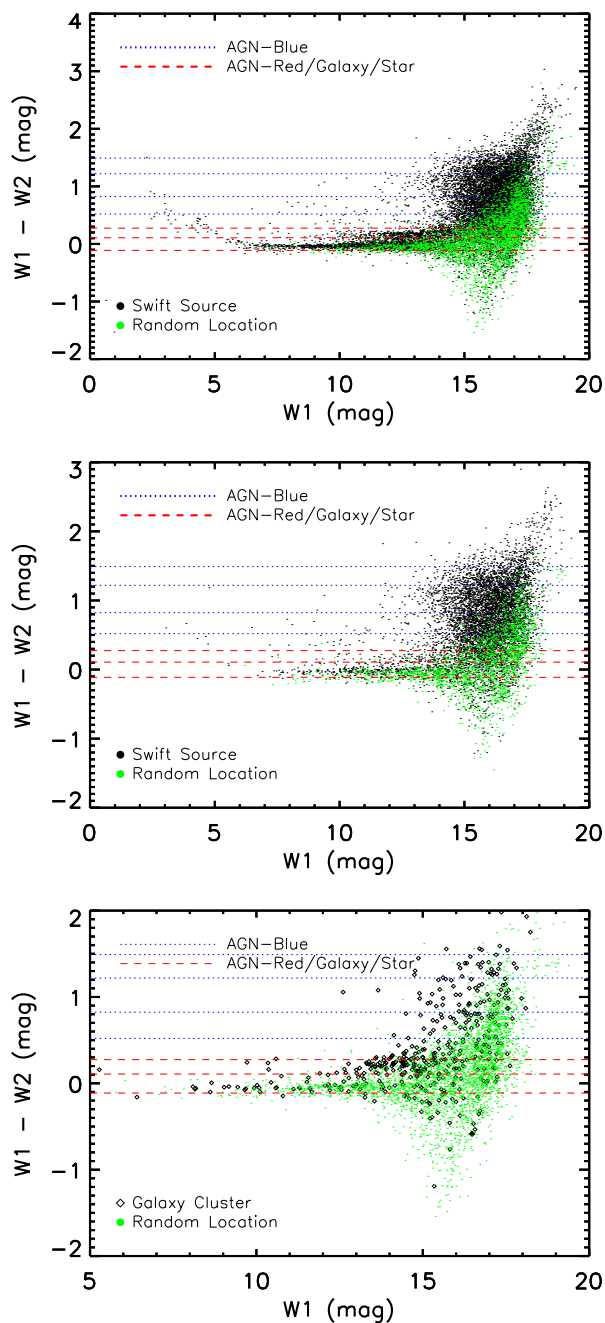


Fig. 10.— *WISE* $W1 - W2$ color versus $W1$ magnitude diagrams for *Swift* sources (black dots), random locations (green dots), and Type-I AGN tracks at $z = 0.5, 1.5, 3.5,$ and 4.5 (blue dotted lines), and early, late, and irregular galaxy tracks (red dashed lines). The top and middle panels show the color-magnitude diagrams for point sources detected in the soft and hard X-ray bands, respectively. The bottom panel shows the color-magnitude diagram for galaxy clusters detected in the soft X-ray band.

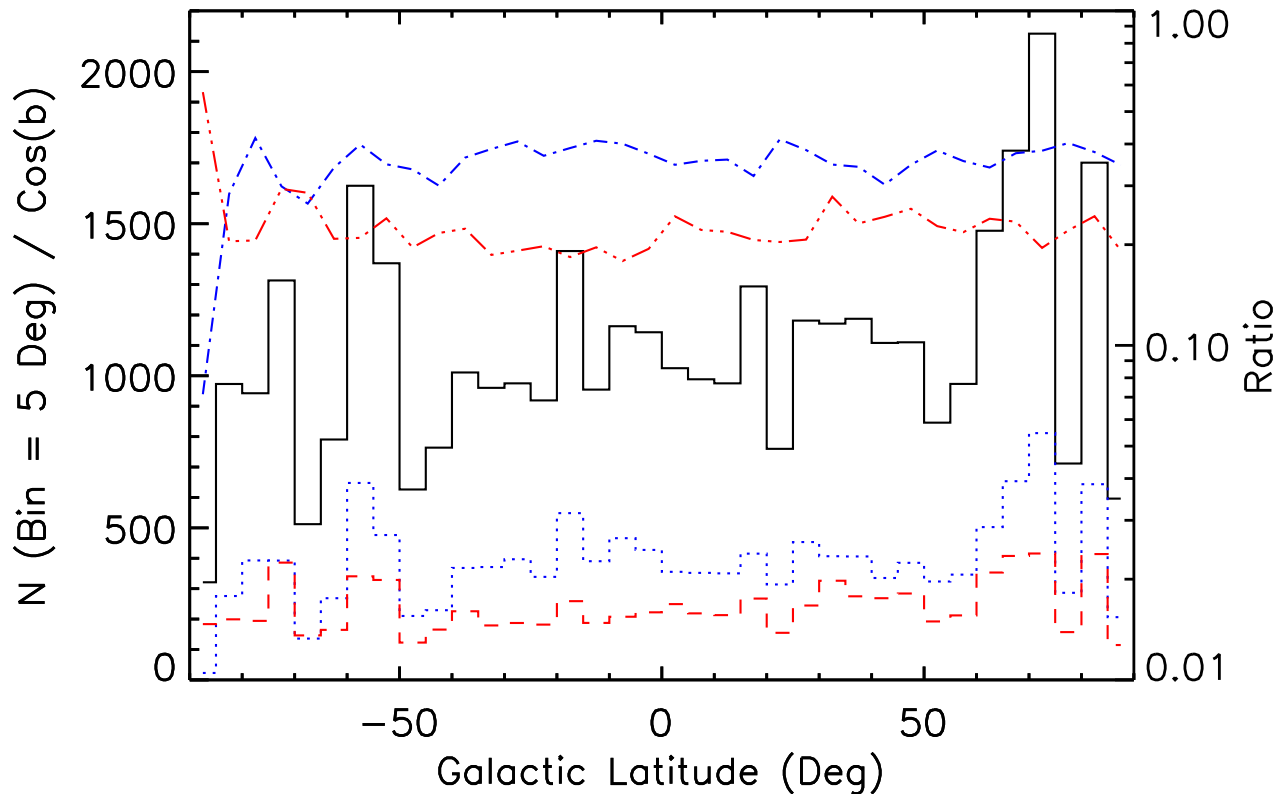


Fig. 11.— Galactic latitude (b) histograms for the total band X-ray sources divided by $\cos b$, where flat distributions are expected for sources distributed randomly on the sky. The black, solid histogram is for all detected sources, the blue, dotted histogram is for the MIR-red AGN, and the red, dashed histogram is for the MIR-blue AGN. The dotted (blue) and dashed (red) lines show the ratios of MIR-red and MIR-blue AGN to all sources in each bin, respectively. The number ratios (blue dot-dashed and red dot-dot-dot-dashed lines) do not show a peak near the Galactic plane, indicating that the catalogs contain few stellar sources.

of Evans et al. (2014) by 0.5 dex, because GRB fields are in general the deeper fields in the *Swift*-XRT data set. For extended sources, at the bright flux end, $> 10^{-13}$ erg cm $^{-2}$ s $^{-1}$, our sample and that of Tundo et al. (2012) have consistent flux distributions both in the shape and normalization; Tundo et al. (2012) only reported a tail of extended sources with fluxes below 10^{-13} erg cm $^{-2}$ s $^{-1}$.

5. Source Number Counts

We calculate the cumulative number counts ($\log(N > S) - \log S$) of galaxy clusters and AGN detected in the survey as

$$N(> S) = \sum_{S_i > S} \frac{1}{\Omega_i C_i}, \quad (2)$$

where S_i is the total flux of the source, Ω_i is the total solid angle of the survey reaching flux S_i and C_i is the incompleteness factor for each source. The survey area as a function of flux is calculated from the exposure maps (dashed and dotted lines in Figure 3), where the areas are normalized to an effective N_H of 5×10^{20} cm $^{-2}$. We model the completeness factor for point sources using Poisson statistics, and we estimate the completeness factor for extended sources based on our simulations (Section 3.1, e.g., Figure 6).

Figures 15, 16 and 17 show the differential number counts for AGN in the total, soft and hard X-ray bands, respectively, and Figure 18 shows the cumulative cluster number counts in the soft X-ray band. We show differential number counts for AGN because we have many sources and this makes the uncertainties in the flux bins independent. For the clusters we show the integral number counts because the differential number counts are noisy and most previous cluster surveys only provide cumulative number counts. The *Swift* differential AGN number counts and cumulative cluster number counts are provided in Tables 8, 9, and 10.

AGN number counts are generally modeled as a broken power-law with a sharp break, and Figures 15, 16 and 17 show that our AGN number counts are consistent with previous measurements in both the total, soft, and hard X-ray bands. Here we use the *Chandra* Deep Field South (CDF-S, Lehmer et al. 2012) and the ChaMP survey (Kim et al. 2007) as the comparison samples. With the large number of sources detected in the *Swift* fields, we can place tighter constraints on the slope of the bright end of number counts than previous studies. We fit the *Swift* differential number counts (dN/dS) of AGN using the standard broken power law model,

$$dN/dS = \begin{cases} K(S/S_{ref})^{-a} & (S \leq f_b) \\ K(f_b/S_{ref})^{b-a}(S/S_{ref})^{-b} & (S > f_b) \end{cases} \quad (3)$$

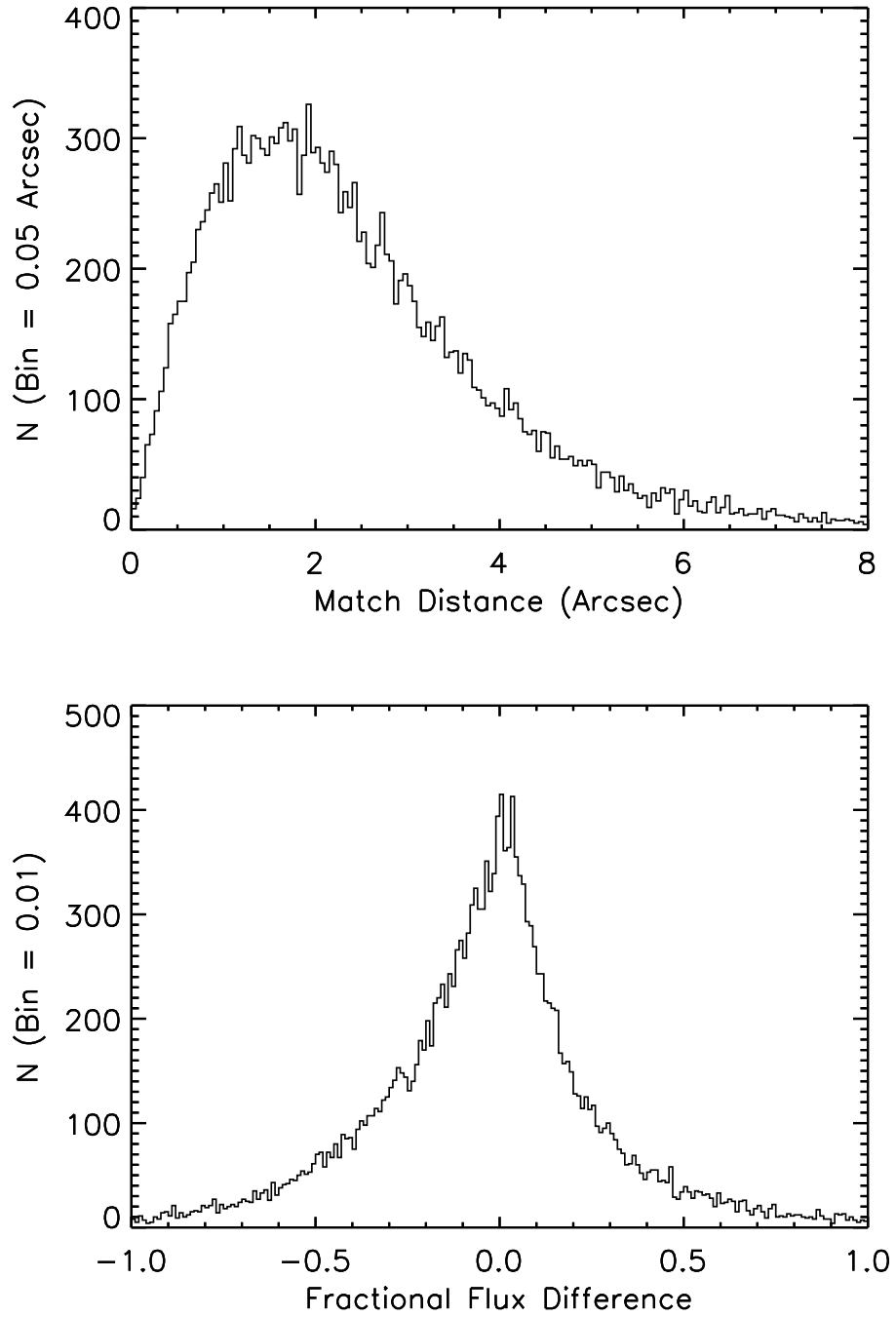


Fig. 12.— Source match distance distribution (top panel) and fractional total flux difference distribution (0.5–8 keV, bottom panel) between the AGN catalog of this paper and Evans et al. (2014).

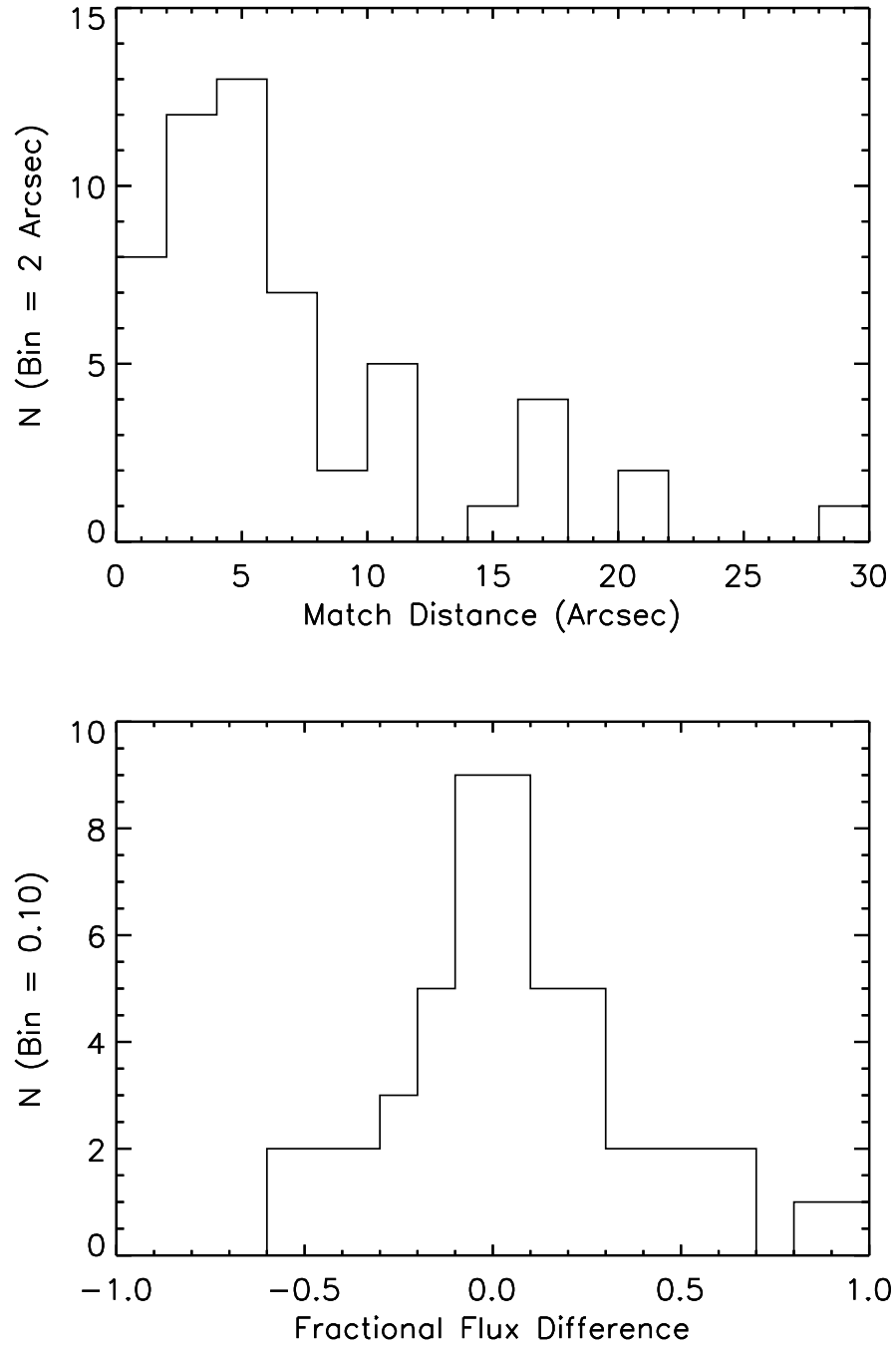


Fig. 13.— Source match distance distribution (top panel) and fractional soft flux difference distribution (0.5–2 keV, bottom panel) between the cluster catalog of this paper and Tundo et al. (2012).

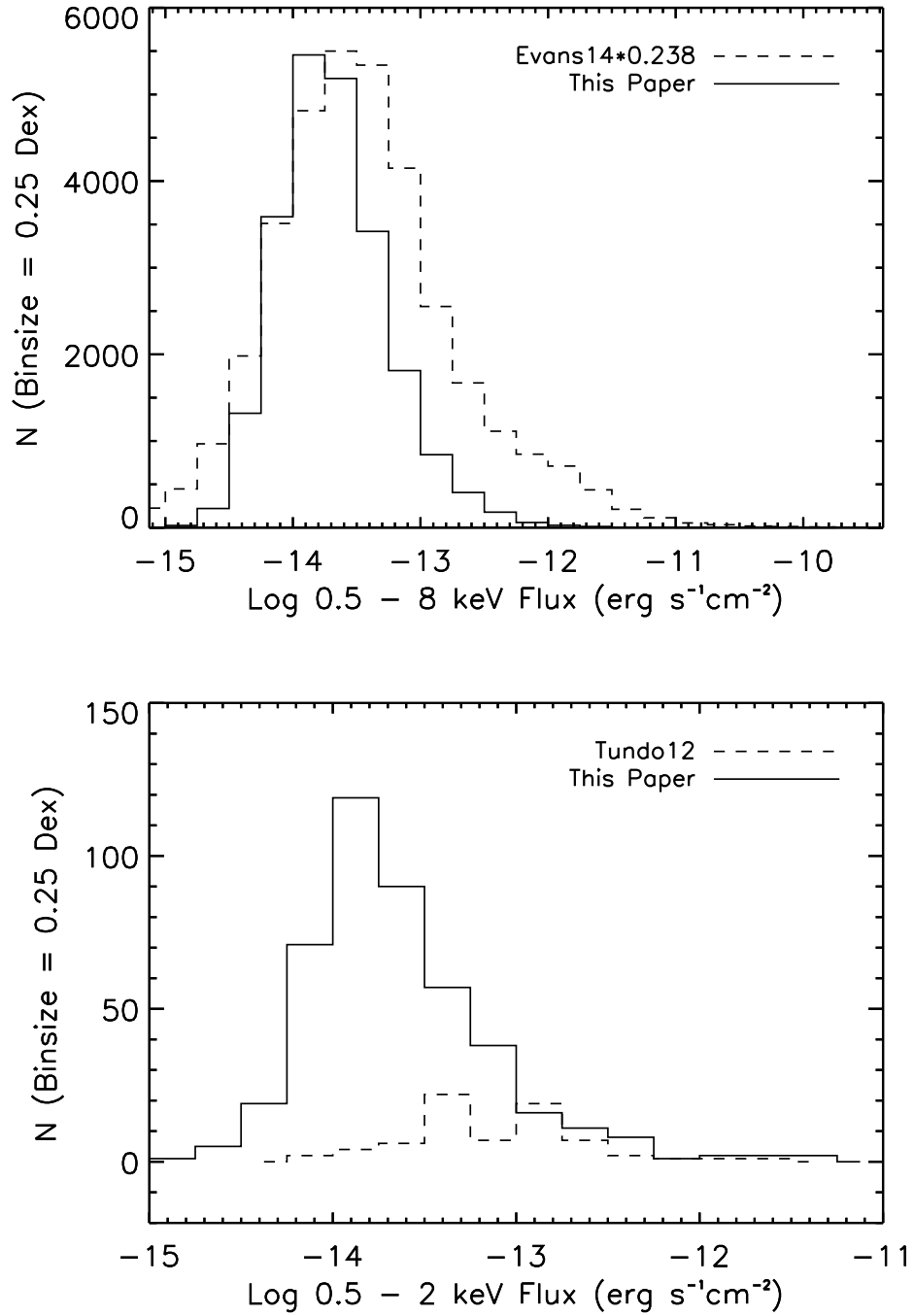


Fig. 14.— Comparisons of the source flux distributions to the AGN catalog of Evans et al. (2014) normalized by a factor of 0.238 (top panel) and to the cluster catalog of Tundo et al. (2012) (bottom panel).

where S_{ref} is a reference flux set to 10^{-14} erg cm $^{-2}$ s $^{-1}$, f_b is the break flux, and K , a and b are the normalization, and power-law indices at the low and high flux ends, respectively. The parameters of the models are provided in Table 11. We fixed the power-law index for faint sources, a , to that measured for the CDF-S since the *Swift* number counts do not extend much below the break. We measure bright end slopes of $b = 2.37 \pm 0.01$, 2.54 ± 0.04 and 2.39 ± 0.14 for the total, soft and hard bands, respectively. The measurement uncertainties are smaller than the corresponding uncertainties from the CDF-S, $b = 2.35 \pm 0.15$, 2.48 ± 0.27 and 2.55 ± 0.17 , and comparable to the ChaMP measurements of $b = 2.48 \pm 0.05$, 2.36 ± 0.05 , and 2.65 ± 0.07 . Our results agree more with the CDF-S results at the bright fluxes and modestly disagree with the ChaMP results.

These uncertainties only represent Poisson errors due to the number of sources. Cosmic variance can be a more important source of differences between surveys due to large scale structures. Using 10^{-14} erg cm $^{-2}$ s $^{-1}$ in the 0.5–2 keV band as a reference, we estimate that the redshift limit for L_X^* AGN with this flux is $z > 4$ because of their rapid positive luminosity evolution (Hasinger et al. 2005). At fixed flux, the survey volume is simply proportional to the survey area, and thus SACS will provide the largest survey volume and the smallest cosmic variance. Based on the cosmic variance estimator of Trenti & Stiavelli (2008), we estimate that the level of cosmic variance in CDF, ChaMP, and SACS are ~ 15 , 2, and 1%, respectively. Thus, the differences between CDF and SACS can be easily explained by cosmic variance; however, the differences between ChaMP and SACS must originate from other sources of systematic uncertainties, such as the source detection and flux estimation methods.

We can approximate the division into Type I and II AGN using the MIR colors of the sources with *WISE* matches. Generally, the objects selected to have red MIR colors will also show broad line spectra (see Kochanek et al. 2012). To maximize purity, we keep only sources matched within 5" although we find no significant differences if we use 8". Here we fix both the faint end slope a and the break flux f_b to the values found for the CDF-S. Not all *Swift* AGN have *WISE* matches, and for simplicity we correct this by multiplicatively increasing the number counts by the inverse of the matched fractions in each bin. This is an over-simplification given any correlation between the X-ray and MIR fluxes. Comparing the number counts between MIR-red and MIR-blue AGN in the total and soft band, we find that there are similar numbers of each, while for the hard band we find that only about 1/3 are MIR-blue. This result is somewhat unexpected because we expected that the spectra of MIR-blue AGN, corresponding to Type II AGN, would be harder because of the higher intrinsic absorption. It is possible that many of the harder, Type II X-ray sources remain mid-IR red, suggesting that the total absorption column densities are modest. Optical (visual) and soft X-ray (keV) opacities are similar for typical dust-to-gas ratios (e.g., Dai & Kochanek

2009; Chen et al. 2013), so the transition from Type I to Type II as an X-ray source will be associated with suppression of the optical signatures of an AGN. However, mid-IR dust opacities are over an order of magnitude lower, so there is an extended range of intermediate column densities ($N_{\text{H}} \sim 10^{23} \text{ cm}^{-2}$), where absorption will produce the optical and X-ray signatures associated with Type II AGN while having little effect on the mid-IR colors. With the large number of sources detected, we can measure the intrinsic absorption by stacking the source events based on the flux bins, and we plan to explore this further in follow-up studies.

For the cluster number counts, we compare the *Swift* cumulative number counts with the composite cumulative number counts from Rosati et al. (2002) which combines the *ROSAT*, CDF-S and *XMM-Newton-COSMOS* field (Finoguenov et al. 2007) results for the soft X-ray band (0.5–2 keV). The number counts of our extended source catalog match these well, strongly indicating that it is dominated by real clusters. We fit the cumulative cluster number counts with a smooth broken power-law model,

$$N(> S) = K \frac{(S/f_b)^{-a}}{(1 + (S/f_b)^c)^{(b-a)/c}}, \quad (4)$$

where f_b is the break flux, $c \equiv 2$ is a fixed “smoothness”, K sets the normalization and a , b are the power-law indices at faint and bright fluxes. We first fit the *Swift* data only and then all available data in Figure 18, where the fitting results are listed in Table 12. Since the *Swift* constraints do not extend below the break of the relation, we fixed the break location and the power law index at faint fluxes to be that found for the global fit using all the data. The two fits are consistent in normalization and the power-law index for bright sources. We find that the power-law index for bright sources is $b = 1.25 \pm 0.04$ and $b = 1.24 \pm 0.01$ using the *Swift* and the combined data, respectively. This is significantly different from Euclidean slope of 1.5, indicating that there is strong source evolution with redshift, as expected for a late-forming population like rich galaxy clusters. At brighter fluxes than probed by SACS, $> 4 \times 10^{-12} \text{ erg cm}^{-2} \text{ s}^{-1}$, the number counts steepen to $b = 1.32 \pm 0.05$ (Ebeling et al. 1998), and the slope reaches the Euclidean value at fluxes above $> 10^{-11} \text{ erg cm}^{-2} \text{ s}^{-1}$ (Ebeling et al. 1998; De Grandi et al. 1999). We also estimate the effects of cosmic variance at a reference flux of $10^{-14} \text{ erg cm}^{-2} \text{ s}^{-1}$, and set a redshift limit of $z < 1.5$ in these estimates, since clusters are lower redshift objects. We find that cosmic variance can contribute ~ 15 and 5% uncertainties for *XMM-Newton-COSMOS* and SACS surveys, respectively, which are consistent with the differences between the number count measurements of the two surveys.

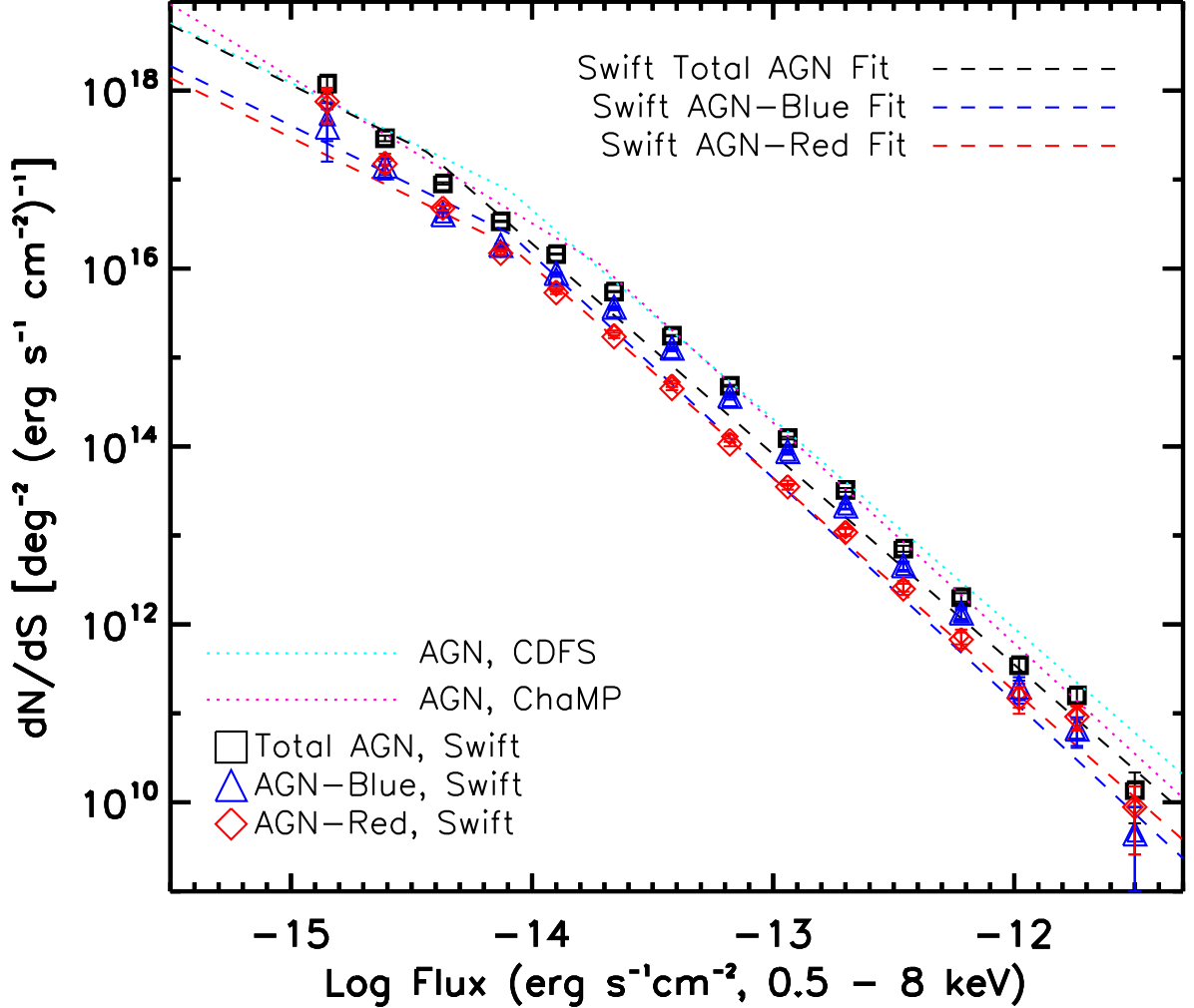


Fig. 15.— Differential number counts for the total band (0.5–8 keV) *Swift* sources for all AGN (black squares), MIR-red AGN (blue triangles, meaning Type I), and MIR-blue AGN (red diamonds, meaning Type II). The larger and smaller symbols (for triangles and diamonds only) are the 5'' and 8'' *WISE* match results, respectively, where we have corrected the incomplete *WISE* detection fractions. The dotted cyan and magenta lines are the best-fit number counts from the CDF-S and ChaMP. The black, blue, and red dashed lines show our fits to the *Swift* number counts for the total, MIR-red, and MIR-blue AGN, respectively. The MIR-blue AGN represent 50% of the total band point source detections.

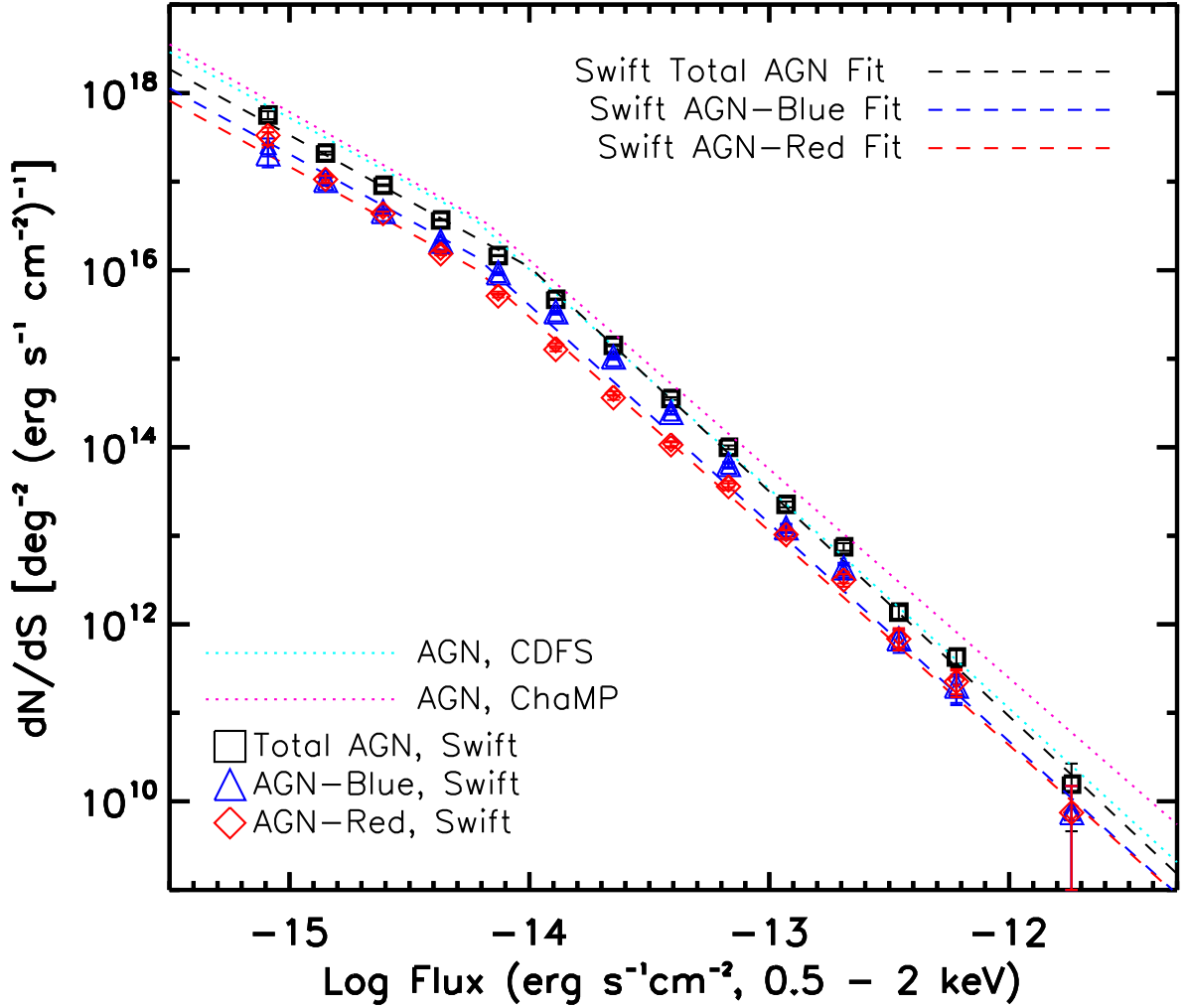


Fig. 16.— Differential number counts for the soft band (0.5–2 keV) *Swift* sources for all AGN (black squares), MIR-red AGN (blue triangles, meaning Type I), and MIR-blue AGN (red diamonds, meaning Type II). The larger and smaller symbols (for triangles and diamonds only) are the 5'' and 8'' *WISE* match results, respectively, where we have corrected the incomplete *WISE* detection fractions. The dotted cyan and magenta lines are the best-fit number counts from the CDF-S and ChaMP. The black, blue, and red dashed lines show our fits to the *Swift* number counts for the total, MIR-red, and MIR-blue AGN, respectively. The MIR-blue AGN represent 50% of the soft band point source detections.

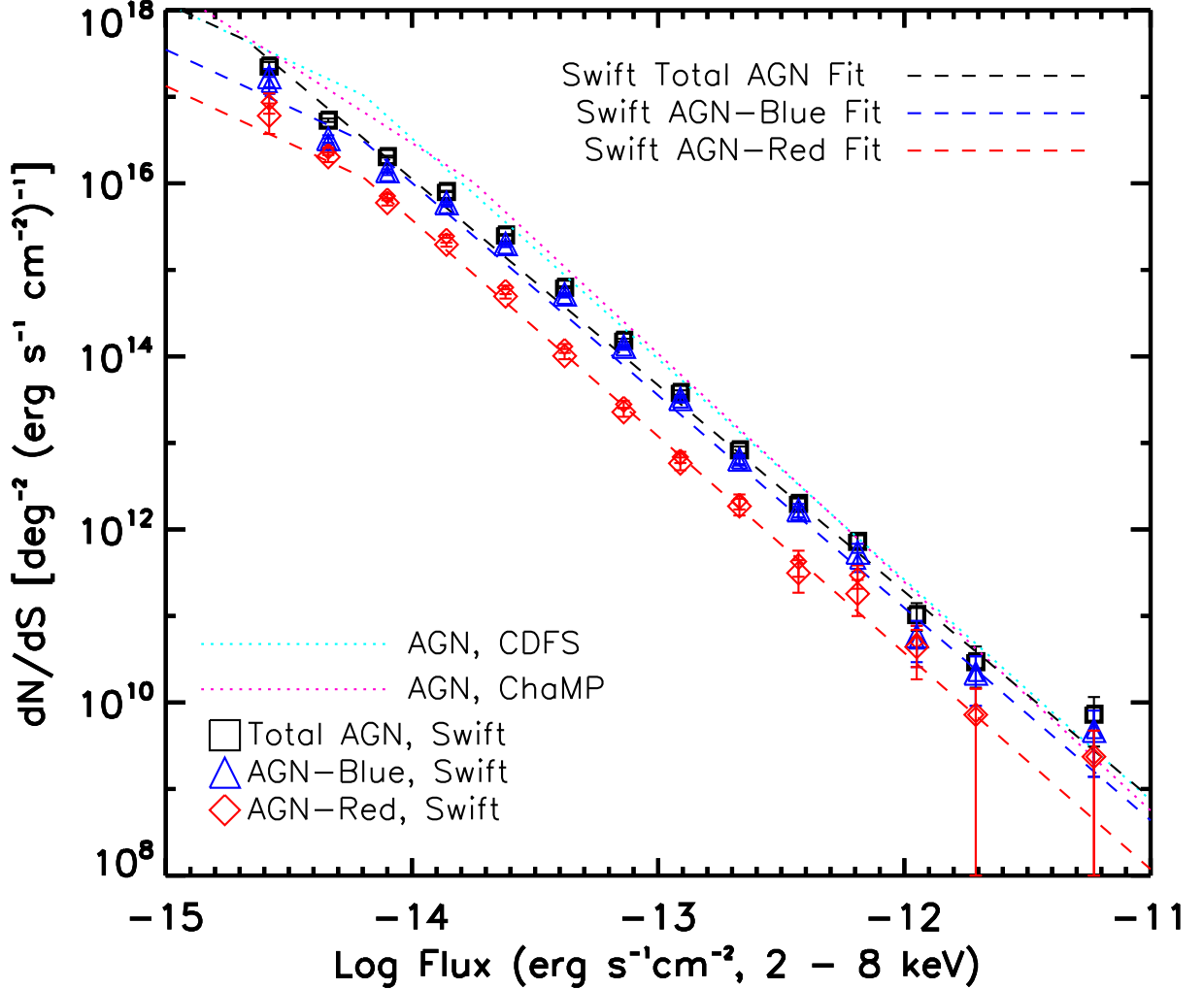


Fig. 17.— Differential number counts for the hard band (2–8 keV) *Swift* survey for all AGN (black squares), MIR-red AGN (blue triangles, meaning Type I), and MIR-blue AGN (red diamonds, meaning Type II). The larger and smaller symbols (for triangles and diamonds only) are the $5''$ and $8''$ *WISE* match results, respectively, where we have corrected the incomplete *WISE* detection fractions. The dotted cyan and magenta lines are the best-fit number counts from the CDF-S and ChaMP. The black, blue, and red dashed lines are our fits to the *Swift* number counts for the total, MIR-red, and MIR-blue AGN, respectively. The MIR-blue AGN represent 25% of the hard band point source detections.

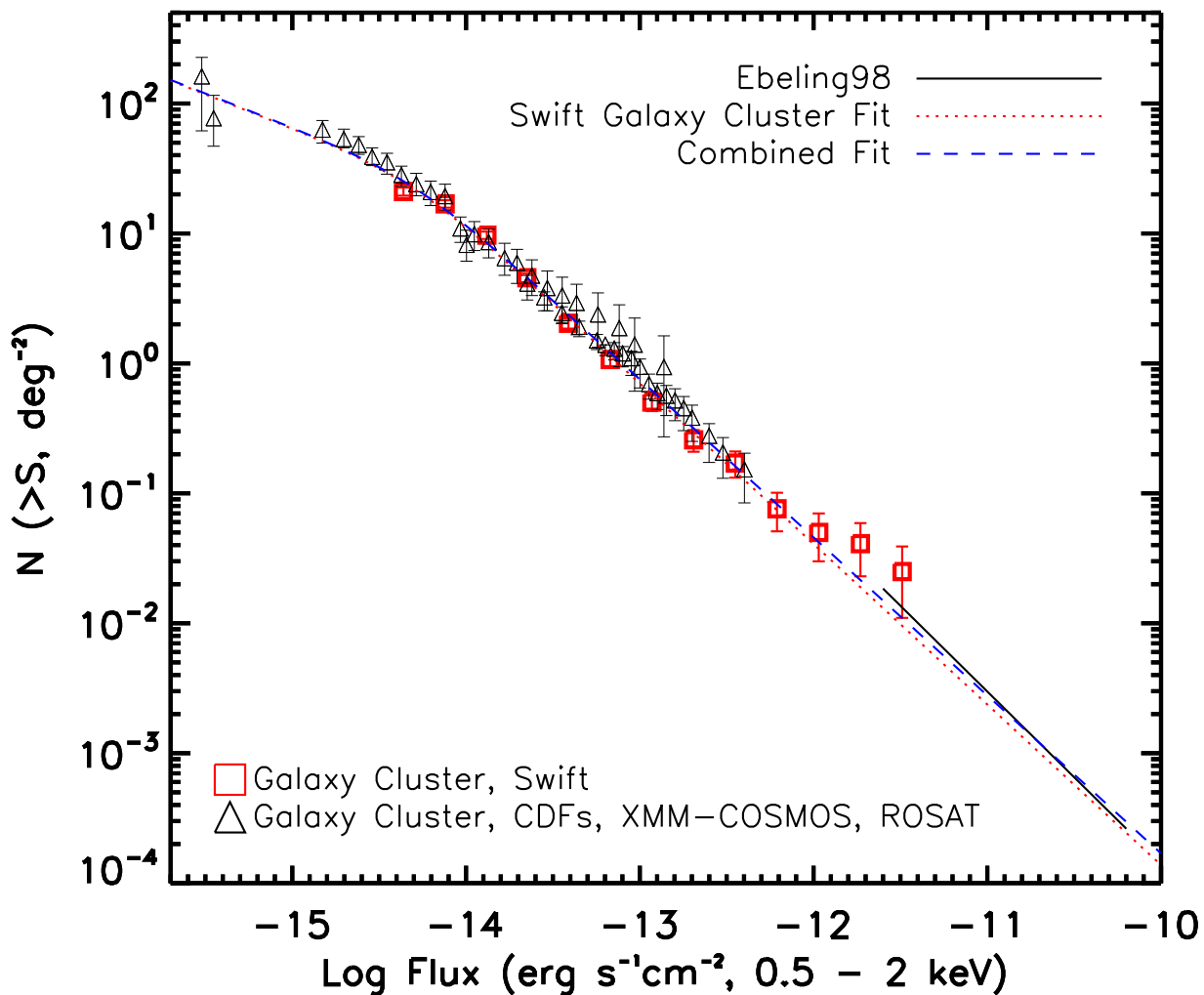


Fig. 18.— Cumulative number counts of galaxy clusters in the 0.5–2 keV band from the *Swift* survey (red squares) as compared to results from the XMM-COSMOS, ROSAT, and CDF-S surveys (black triangles and the black solid line). The red dotted line shows the broken power-law fit to the *Swift* data only, and the blue dashed line shows the fit to the combined data with fluxes lower than $4 \times 10^{-12} \text{ erg cm}^{-2} \text{ s}^{-1}$.

6. Discussion

Swift observations of GRB fields form an excellent serendipitous soft X-ray survey with a medium depth and wide sky coverage. For example, the total number of sources detected in our survey ($\sim 22,000$) is larger than the RASS sample ($\sim 18,000$, Voges et al. 1999). The large number of sources enables us to more accurately measure source number counts, especially for bright sources and with few systematics due to cosmic variance. Since GRBs are not correlated with other sources, there is little selection bias for extragalactic objects. This is very different from serendipitous surveys based on *Chandra* and *XMM-Newton* where many of the fields are selected to study either clusters or AGN. In addition, the relative uniformity of the *Swift*-XRT PSF across its field of view allows for much more uniform source detection and characterization than those for *ROSAT*, *Chandra*, or *XMM-Newton*, where the PSF strongly or moderately depends on the off-axis angle.

The next step is to study these sources in detail using multi-wavelength data. In this paper, we matched the sources to the *WISE* all-sky catalog and found 15,100 matches of the X-ray sources. We can use the *WISE* $W1 - W2$ color as a proxy for separating the sources into Type I (MIR-red sources) and Type II (MIR-blue sources) since red MIR sources are typically found to be broad line quasars (see Kochanek et al. 2012). In the total and soft band about 50% of the AGN are Type II, similar to the distributions seen in Chung et al. (2014). We plan to extend these comparisons using the $\sim 9000 \text{ deg}^2$ coverage of the SDSS. However, more complete identifications across the full sky will require the new generation of optical surveys such as PanSTARRS, DES, and LSST.

The depth and areal coverage of the *Swift* serendipitous survey is well suited for galaxy cluster surveys outside the local universe, reaching $z \sim 1$ for massive clusters. In this paper we have identified 442 cluster candidates as extended X-ray sources. Their measured number counts are consistent with previous studies and they show few matches to red MIR sources, so the contamination by AGN is small. Compared to optical cluster surveys where the numbers of candidates can exceed 50,000 (Hao et al. 2010), the total numbers of X-ray selected clusters are relatively small. For example, Piffaretti et al. (2011) compiled a meta X-ray cluster catalog with 1,743 clusters. Our *Swift* cluster sample significantly expands the number of X-ray selected clusters, and it is one of the largest uniformly selected cluster samples. Based on the models of cluster mass functions as a function of redshift (e.g., Tinker et al. 2008) and the flux limits of our survey, we expect that the peak of our cluster redshift distribution is at $z \sim 0.5$. In Griffin et al. (2015), we use the SDSS survey data to identify roughly half of clusters in the SDSS regions as $z < 0.5$ clusters, consistent with the model prediction. We expect the remainder are higher redshift clusters, but the SDSS data is too shallow to provide robust photometric redshifts. We have started dedicated optical follow-up

programs to further measure the photometric redshift of the *Swift* clusters, and we expect to significantly increase the number of X-ray selected clusters at $z > 0.5$. The sample could be expanded further by relaxing the 3σ selection limit in regions where deep optical imaging data is available to clearly identify optical over-densities or red galaxy sequences.

Since the *Swift*-XRT is still routinely observing GRB afterglows, the sample size will continue to increase. However, the current analysis already uses ~ 9 yr of the data through mid-2013, so the sample size is unlikely to double and the final available area will likely be 160–200 deg² with equivalent on-axis exposure times exceeding 10 ks. *Swift* has spent a significant amount of observing time on sources other than GRBs, and using all these observations could increase the sample by a factor of 5 at the price of introducing significantly more complex selection effects. Future dedicated wide-field X-ray surveys will greatly improve the statistics of the X-ray source properties. For example, *eROSITA* plans to perform three surveys (all-sky, medium, and deep) within the next 5–10 years. The current *Swift* serendipitous GRB field data has one third the sky coverage of the designed *eROSITA* deep fields and will eventually reach one half to two-thirds the size. This makes our *Swift* survey an excellent prototype for the wide-field X-ray surveys of the future.

We thank the anonymous referee for helpful comments. We acknowledge the financial support from the NASA ADAP program NNX11AD09G and NSF grant AST-1413056.

REFERENCES

- Assef, R. J., Stern, D., Kochanek, C. S., et al. 2013, *ApJ*, 772, 26
- Böhringer, H., Schuecker, P., Guzzo, L., et al. 2004, *A&A*, 425, 367
- Brandt, W. N., Alexander, D. M., Hornschemeier, A. E., et al. 2001, *AJ*, 122, 2810
- Brandt, W. N., & Hasinger, G. 2005, *ARA&A*, 43, 827
- Burenin, R. A., Vikhlinin, A., Hornstrup, A., et al. 2007, *ApJS*, 172, 561
- Burrows, D. N., Hill, J. E., Nousek, J. A., et al. 2005, *Space Sci. Rev.*, 120, 165
- Burke, D. J., Collins, C. A., Sharples, R. M., et al. 1997, *ApJ*, 488, L83
- Campana, S., Lazzati, D., Panzera, M. R., & Tagliaferri, G. 1999, *ApJ*, 524, 423
- Castander, F. J., Bower, R. G., Ellis, R. S., et al. 1995, *Nature*, 377, 39

- Chen, B., Dai, X., Kochanek, C. S., & Chartas, G. 2013, arXiv:1306.0008
- Chung, S. M., Kochanek, C. S., Assef, R., et al. 2014, arXiv:1402.5420
- Clerc, N., Pierre, M., Pacaud, F., & Sadibekova, T. 2012, MNRAS, 423, 3545
- Collins, C. A., Burke, D. J., Romer, A. K., Sharples, R. M., & Nichol, R. C. 1997, ApJ, 479, L117
- Dai, X., Kochanek, C. S., & Morgan, N. D. 2007, ApJ, 658, 917
- Dai, X., Kochanek, C. S., Chartas, G., et al. 2010, ApJ, 709, 278
- Dai, X., & Kochanek, C. S. 2009, ApJ, 692, 677
- De Grandi, S., Böhringer, H., Guzzo, L., et al. 1999, ApJ, 514, 148
- D’Elia, V., Perri, M., Puccetti, S., et al. 2013, A&A, 551, A142
- Dickey, J. M., & Lockman, F. J. 1990, ARA&A, 28, 215
- Donahue, M., Mack, J., Scharf, C., et al. 2001, ApJ, 552, L93
- Ebeling, H., Edge, A. C., Böhringer, H., et al. 1998, MNRAS, 301, 881
- Ebeling, H., Edge, A. C., Allen, S. W., et al. 2000, MNRAS, 318, 333
- Evans, P. A., Osborne, J. P., Beardmore, A. P., et al. 2014, ApJS, 210, 8
- Fassbender, R., Böhringer, H., Nastasi, A., et al. 2011, New Journal of Physics, 13, 125014
- Finoguenov, A., Guzzo, L., Hasinger, G., et al. 2007, ApJS, 172, 182
- Gehrels, N., Chincarini, G., Giommi, P., et al. 2004, ApJ, 611, 1005
- Gorjian, V., Brodwin, M., Kochanek, C. S., et al. 2008, ApJ, 679, 1040
- Hao, J., McKay, T. A., Koester, B. P., et al. 2010, ApJS, 191, 254
- Hasinger, G., Boese, G., Predehl, P., Turner, T. J., Yusaf, R., George, I. M., and Rohrbach, G. 1994, Legacy 4, 40, MPE/OGIP Calibration Memo CAL/ROS/93-015
- Hasinger, G., Miyaji, T., & Schmidt, M. 2005, A&A, 441, 417
- Henry, J. P., Gioia, I. M., Mullis, C. R., et al. 2001, ApJ, 553, L109
- Jansen, F., Lumb, D., Altieri, B., et al. 2001, A&A, 365, L1

- Jones, L. R., Scharf, C., Ebeling, H., et al. 1998, *ApJ*, 495, 100
- Kim, D.-W., Cameron, R. A., Drake, J. J., et al. 2004, *ApJS*, 150, 19
- Kim, M., Wilkes, B. J., Kim, D.-W., et al. 2007, *ApJ*, 659, 29
- Kochanek, C. S., Eisenstein, D. J., Cool, R. J., et al. 2012, *ApJS*, 200, 8
- Koester, B. P., McKay, T. A., Annis, J., et al. 2007, *ApJ*, 660, 239
- Liu, T., Tozzi, P., Tundo, E., et al. 2013, *A&A*, 549, A143
- Lloyd-Davies, E. J., Romer, A. K., Mehrtens, N., et al. 2011, *MNRAS*, 418, 14
- Marriage, T. A., Acquaviva, V., Ade, P. A. R., et al. 2011, *ApJ*, 737, 61
- Moretti, A., Campana, S., Mineo, T., et al. 2005, *Proc. SPIE*, 5898, 360
- Murray, S. S., Kenter, A., Forman, W. R., et al. 2005, *ApJS*, 161, 1
- Neumann, D. M., & Arnaud, M. 1999, *A&A*, 348, 711
- Osmond, J. P. F., & Ponman, T. J. 2004, *MNRAS*, 350, 1511
- Perlman, E. S., Horner, D. J., Jones, L. R., et al. 2002, *ApJS*, 140, 265
- Pierre, M., Valtchanov, I., Altieri, B., et al. 2004, *J. Cosmology Astropart. Phys.*, 9, 11
- Piffaretti, R., Arnaud, M., Pratt, G. W., Pointecouteau, E., & Melin, J.-B. 2011, *A&A*, 534, A109
- Planck Collaboration, Ade, P. A. R., Aghanim, N., et al. 2014, *A&A*, 571, AA29
- Puccetti, S., Capalbi, M., Giommi, P., et al. 2011, *A&A*, 528, A122
- Rosati, P., Borgani, S., & Norman, C. 2002, *ARA&A*, 40, 539
- Rosati, P., della Ceca, R., Norman, C., & Giacconi, R. 1998, *ApJ*, 492, L21
- Rosati, P., Della Ceca, R., Burg, R., Norman, C., & Giacconi, R. 1995, *ApJ*, 445, L11
- Sanderson, A. J. R., Ponman, T. J., Finoguenov, A., Lloyd-Davies, E. J., & Markevitch, M. 2003, *MNRAS*, 340, 989
- Scharf, C. A., Jones, L. R., Ebeling, H., et al. 1997, *ApJ*, 477, 79
- Stern, D., Eisenhardt, P., Gorjian, V., et al. 2005, *ApJ*, 631, 163

- Skrutskie, M. F., Cutri, R. M., Stiening, R., et al. 2006, *AJ*, 131, 1163
- Trenti, M., & Stiavelli, M. 2008, *ApJ*, 676, 767
- Tundo, E., Moretti, A., Tozzi, P., et al. 2012, *A&A*, 547, A57
- Vikhlinin, A., McNamara, B. R., Forman, W., et al. 1998, *ApJ*, 502, 558
- Vikhlinin, A., Kravtsov, A. V., Burenin, R. A., et al. 2009, *ApJ*, 692, 1060
- Voges, W., Aschenbach, B., Boller, T., et al. 1999, *A&A*, 349, 389
- Watson, M. G., Schröder, A. C., Fyfe, D., et al. 2009, *A&A*, 493, 339
- Weisskopf, M. C., Brinkman, B., Canizares, C., et al. 2002, *PASP*, 114, 1
- Weisskopf, M. C., Wu, K., Trimble, V., et al. 2007, *ApJ*, 657, 1026
- Wright, E. L., Eisenhardt, P. R. M., Mainzer, A. K., et al. 2010, *AJ*, 140, 1868
- Xu, H., Jin, G., & Wu, X.-P. 2001, *ApJ*, 553, 78
- Xue, Y. Q., Luo, B., Brandt, W. N., et al. 2011, *ApJS*, 195, 10

Table 1. *Swift* Sources Detected in the Total X-ray (0.2–10 keV) Band

Name	RA (J2000) (deg)	DEC (J2000) (deg)	Count Rate (0.2–10 keV) (10^{-3} cnt s $^{-1}$)	Flux (0.5–8 keV) (10^{-14} erg cm $^{-2}$ s $^{-1}$)	Exposure (sec)	W1 (mag)	W2 (mag)	W3 (mag)	W4 (mag)	Match R (arcsec)
SACS J000002.1+443056	0.0082± 0.0003	44.5156± 0.0002	0.900± 0.106	4.20	100290	15.73	15.18	11.59	8.89	3.41
SACS J000003.8+442911	0.0149± 0.0003	44.4864± 0.0002	0.631± 0.092	2.99	95614	15.53	14.61	11.82	9.27	0.73
SACS J000003.9+444147	0.0155± 0.0004	44.6964± 0.0002	0.454± 0.080	2.16	99454	99.00	99.00	99.00	99.00	99.00
SACS J000005.2+443534	0.0208± 0.0003	44.5927± 0.0002	0.911± 0.103	4.21	108539	16.37	15.28	12.30	9.43	3.23
SACS J000009.6+444130	0.0390± 0.0003	44.6916± 0.0002	0.353± 0.070	1.71	103680	16.30	15.88	13.06	9.35	0.72
SACS J000010.4-344341	0.0427± 0.0007	-34.7280± 0.0005	0.911± 0.274	3.51	14190	13.81	13.23	9.81	7.78	4.64
SACS J000014.8-344322	0.0613± 0.0007	-34.7227± 0.0003	0.407± 0.151	1.64	21921	16.08	15.45	12.87	9.18	3.74
SACS J000018.1-344836	0.0748± 0.0004	-34.8099± 0.0002	1.766± 0.296	6.67	22194	16.29	15.81	12.44	9.03	2.02
SACS J000019.4-345317	0.0803± 0.0006	-34.8878± 0.0003	0.564± 0.209	2.28	15237	17.50	16.60	12.34	8.72	1.87
SACS J000021.2+444342	0.0877± 0.0003	44.7283± 0.0002	0.797± 0.104	3.72	94366	12.35	12.37	12.07	8.81	3.64

Note. — Table 1 is published in its entirety in the electronic edition of the *Astrophysical Journal*. A portion is shown here for guidance regarding its form and content.

Table 2. *Swift* Sources Detected in the Soft X-Ray (0.5–2 keV) Band

Name	RA (J2000) (deg)	DEC (J2000) (deg)	Count Rate (0.5–2 keV) (10^{-3} cnt s $^{-1}$)	Flux (0.5–2 keV) (10^{-14} erg cm $^{-2}$ s $^{-1}$)	Exposure (sec)	W1 (mag)	W2 (mag)	W3 (mag)	W4 (mag)	Match R (arcsec)
SACS J000002.3+443056	0.0088± 0.0003	44.5155± 0.0002	0.536± 0.078	1.53	100372	15.73	15.18	11.59	8.89	3.22
SACS J000003.7+442911	0.0147± 0.0004	44.4863± 0.0002	0.374± 0.068	1.09	95634	15.53	14.61	11.82	9.27	1.13
SACS J000004.1+444147	0.0163± 0.0005	44.6965± 0.0002	0.349± 0.064	1.02	99552	99.00	99.00	99.00	99.00	99.00
SACS J000005.4+443537	0.0216± 0.0003	44.5935± 0.0002	0.588± 0.078	1.71	108672	16.37	15.28	12.30	9.43	0.99
SACS J000009.5+444129	0.0387± 0.0005	44.6914± 0.0003	0.258± 0.056	0.74	103607	16.30	15.88	13.06	9.35	0.91
SACS J000014.2+443105	0.0585± 0.0008	44.5181± 0.0004	0.081± 0.034	0.25	102784	15.81	15.91	12.48	9.38	6.66
SACS J000018.3-344837	0.0756± 0.0005	-34.8100± 0.0003	0.973± 0.215	2.07	22345	16.29	15.81	12.44	9.03	1.16
SACS J000021.2+444340	0.0874± 0.0004	44.7277± 0.0003	0.508± 0.079	1.45	94517	12.35	12.37	12.07	8.81	4.31
SACS J000024.3+444057	0.1004± 0.0004	44.6825± 0.0004	0.063± 0.029	0.21	104580	16.10	17.16	13.04	9.40	4.02
SACS J000025.0+443636	0.1035± 0.0003	44.6099± 0.0002	0.649± 0.081	1.84	113763	12.06	11.96	11.94	9.18	1.74

Note. — Table 2 is published in its entirety in the electronic edition of the *Astrophysical Journal*. A portion is shown here for guidance regarding its form and content.

Table 3. *Swift* Sources Detected in the Hard X-ray (2–10 keV) Band

Name	RA (J2000) (deg)	DEC (J2000) (deg)	Count Rate (2–10 keV) (10^{-3} cnt s $^{-1}$)	Flux (2–8 keV) (10^{-14} erg cm $^{-2}$ s $^{-1}$)	Exposure (sec)	W1 (mag)	W2 (mag)	W3 (mag)	W4 (mag)	Match R (arcsec)
SACS J000002.0+443053	0.0075± 0.0006	44.5148± 0.0004	0.248± 0.057	2.04	100065	15.73	15.18	11.59	8.89	2.56
SACS J000003.7+442910	0.0145± 0.0003	44.4861± 0.0003	0.219± 0.052	1.89	95350	15.53	14.61	11.82	9.27	2.14
SACS J000005.0+443532	0.0200± 0.0004	44.5922± 0.0003	0.245± 0.054	2.01	108319	16.37	15.28	12.30	9.43	5.53
SACS J000010.3-344341	0.0424± 0.0004	-34.7279± 0.0006	0.467± 0.187	4.20	14126	13.81	13.23	9.81	7.78	4.26
SACS J000014.9-344321	0.0616± 0.0007	-34.7224± 0.0002	0.416± 0.144	3.59	21939	16.08	15.45	12.87	9.18	3.46
SACS J000018.1-344837	0.0748± 0.0008	-34.8101± 0.0004	0.275± 0.119	2.37	22288	16.29	15.81	12.44	9.03	1.68
SACS J000021.1+444339	0.0870± 0.0005	44.7274± 0.0003	0.193± 0.051	1.65	94927	12.35	12.37	12.07	8.81	4.88
SACS J000022.8+443004	0.0942± 0.0007	44.5011± 0.0004	0.107± 0.038	0.92	105265	16.20	15.72	12.11	9.26	10.20
SACS J000027.0+443114	0.1115± 0.0003	44.5205± 0.0006	0.092± 0.033	0.82	111900	13.81	13.51	12.87	8.93	2.35
SACS J000038.9+443747	0.1614± 0.0005	44.6298± 0.0003	0.308± 0.061	2.53	102187	14.69	14.78	13.00	8.99	3.65

Note. — Table 3 is published in its entirety in the electronic edition of the *Astrophysical Journal*. A portion is shown here for guidance regarding its form and content.

Table 4. *Swift* Extended Source Candidates Detected in the Soft X-ray Band (0.5–2 keV)

Name	RA (J2000) (deg)	DEC (J2000) (deg)	Core Size (arcsec)	Extent (arcsec)	Count Rate (0.5–2 keV) (10^{-3} cnt s $^{-1}$)	Flux ^a (0.5–2 keV)	Bkg ^b Rate	Off-Axis Angle (arcmin)	Exposure (sec)	GRB Field
SWCL J000131.7+444414	0.3813	44.7373	15.4	50.7	1.068± 0.159	2.67	1.97	11.3	42004	grb101225a
SWCL J000251.5-525825	0.7139	-52.9734	13.1	22.4	0.211± 0.026	0.41	2.32	6.6	304365	grb070110
SWCL J000314.3-525514	0.8088	-52.9203	32.5	83.7	2.420± 0.088	4.69	2.22	5.6	314164	grb070110
SWCL J000323.8-525355	0.8483	-52.8985	45.4	104.9	3.868± 0.113	7.49	2.23	6.2	302754	grb070110
SWCL J000344.2-530152	0.9332	-53.0310	41.1	62.5	1.034± 0.058	2.00	2.23	2.5	310255	grb070110
SWCL J000755.7-295503	1.9822	-29.9172	13.9	46.0	0.426± 0.087	0.81	1.57	8.6	56789	grb070611
SWCL J001004.8+475139	2.5196	47.8615	12.5	31.8	0.408± 0.059	1.05	1.88	8.1	115977	grb100802a
SWCL J001011.0+475353	2.5455	47.8986	18.6	36.5	0.467± 0.066	1.21	1.84	10.5	105736	grb100802a
SWCL J001100.4+474827	2.7515	47.8079	11.9	31.8	0.320± 0.064	0.83	1.82	12.1	78166	grb100802a
SWCL J001338.0-282923	3.4084	-28.4895	18.5	48.3	0.935± 0.196	1.81	2.19	14.9	24303	grb070721a

^aThe flux has the unit of 10^{-14} erg cm $^{-2}$ s $^{-1}$.

^bThe background count rate has the unit of 10^{-4} cnt s $^{-1}$ arcmin $^{-2}$.

Note. — Table 4 is published in its entirety in the electronic edition of the *Astrophysical Journal*. A portion is shown here for guidance regarding its form and content.

Table 5. Cluster Detection Probability

Net Photons	Background Level ^a	Redshift			
		$z = 0.2$	$z = 0.6$	$z = 1.0$	$z = 1.4$
20	0.0025	0.8054	0.4725	0.3638	0.3351
20	0.0041	0.7885	0.4543	0.3467	0.3178
20	0.0068	0.7638	0.4277	0.3270	0.3000
20	0.0113	0.7215	0.3923	0.2971	0.2711
20	0.0187	0.6572	0.3379	0.2554	0.2343
20	0.0308	0.5476	0.2636	0.1971	0.1809
20	0.0509	0.4232	0.1923	0.1412	0.1285
20	0.0842	0.2818	0.1225	0.0897	0.0833
20	0.1392	0.1777	0.0781	0.0599	0.0529
20	0.2300	0.1009	0.0460	0.0355	0.0333

^aThe background level is in units of cnts pixel⁻¹.

Note. — We assumed $R_c = 0.1$ Mpc and $\beta = 0.6$ for the simulation, corresponding to a total mass of $\sim 2 \times 10^{14} M_\odot$ and close to the mass limit of our survey. Table 5 is published in its entirety in the electronic edition of the *Astrophysical Journal*. A portion is shown here for guidance regarding its form and content.

Table 6. Comparison Between Independent *Swift* XRT Catalogs

Catalog Type	Catalog One	Catalog Two	Number of Matches	Match Dis. (arcsec)	Median Fractional Flux Difference ^a	Standard Deviation ^b
AGN	This Paper	Puccette11	8300	2.17	1.02	0.17
AGN	This Paper	E’Dlia13	8988	2.00	0.53	0.21
AGN	This Paper	Evans14	18861	2.08	0.96	0.17
AGN	Puccette11	E’Dlia13	5182	1.54	0.55	0.21
AGN	Puccette11	Evans14	9091	1.32	1.02	0.20
AGN	E’Dlia13	Evans14	79418	2.28	1.27	0.39
Cluster	This Paper	Tundo12	55	5.20	0.97	0.15

^aThe fractional flux difference is defined as $(\text{Flux}_{\text{cat}2} - \text{Flux}_{\text{cat}1})/\text{Flux}_{\text{cat}1}$.

^bThe standard deviation of the fractional flux difference.

Note. — The fluxes are calibrated to 0.5–8 keV for AGN and 0.5–2 keV for clusters.

Table 7. *Swift* Differential AGN Number Counts in the Total X-ray Band (0.5–8 keV)

log S (erg cm ⁻² s ⁻¹)	dN/dS						Area (Deg ²)
	<i>Swift</i> -All	uncertainty	<i>Swift-WISE</i> Type I	uncertainty	<i>Swift-WISE</i> Type II	uncertainty ^a	
-14.85	1.20e+18	2.84e+17	4.97e+17	2.26e+17	7.23e+17	2.69e+17	2.802e-2
-14.61	2.91e+17	2.11e+16	1.23e+17	2.24e+16	1.69e+17	2.56e+16	6.818e-1
-14.37	9.05e+16	2.62e+15	4.02e+16	2.57e+15	4.84e+16	2.77e+15	7.042e+0
-14.13	3.39e+16	5.90e+14	1.69e+16	5.71e+14	1.64e+16	5.73e+14	2.776e+1
-13.90	1.45e+16	1.98e+14	8.27e+15	1.97e+14	6.01e+15	1.70e+14	5.742e+1
-13.66	5.50e+15	7.69e+13	3.47e+15	7.40e+13	1.95e+15	5.60e+13	8.074e+1
-13.42	1.75e+15	2.97e+13	1.20e+15	2.83e+13	5.29e+14	1.90e+13	9.756e+1
-13.18	4.80e+14	1.11e+13	3.46e+14	1.04e+13	1.29e+14	6.46e+12	1.080e+2
-12.94	1.24e+14	4.13e+12	8.46e+13	3.73e+12	3.87e+13	2.53e+12	1.150e+2
-12.70	3.24e+13	1.57e+12	2.09e+13	1.39e+12	1.13e+13	1.02e+12	1.191e+2
-12.46	7.10e+12	5.51e+11	4.38e+12	4.59e+11	2.70e+12	3.61e+11	1.214e+2
-12.22	2.02e+12	2.22e+11	1.28e+12	1.83e+11	7.35e+11	1.39e+11	1.227e+2
-11.98	3.47e+11	6.95e+10	1.80e+11	5.21e+10	1.65e+11	4.99e+10	1.239e+2
-11.74	1.59e+11	3.56e+10	6.34e+10	2.24e+10	9.51e+10	2.74e+10	1.247e+2
-11.50	1.37e+10	7.92e+09	4.43e+09	4.43e+09	8.86e+09	6.26e+09	1.251e+2

^adN/dS has the unit of Deg⁻² (erg cm⁻² s⁻¹)⁻¹.

Table 8. *Swift* Differential AGN Number Counts in the Soft X-ray Band (0.5–2 keV)

log S (erg cm ⁻² s ⁻¹)	dN/dS						Area (Deg ²)
	<i>Swift</i> -All	uncertainty	<i>Swift-WISE</i> Type I	uncertainty	<i>Swift-WISE</i> Type II	uncertainty ^a	
-15.09	5.66e+17	5.84e+16	2.50e+17	5.71e+16	3.02e+17	5.93e+16	5.10e-1
-14.85	2.10e+17	7.71e+15	9.84e+16	8.20e+15	1.13e+17	8.65e+15	5.79e+0
-14.61	9.12e+16	1.89e+15	4.39e+16	1.78e+15	4.67e+16	1.86e+15	2.23e+1
-14.37	3.69e+16	5.93e+14	2.07e+16	5.78e+14	1.60e+16	5.15e+14	4.92e+1
-14.13	1.46e+16	2.27e+14	8.99e+15	2.15e+14	5.54e+15	1.69e+14	7.26e+1
-13.89	4.69e+15	8.64e+13	3.23e+15	8.14e+13	1.44e+15	5.46e+13	9.04e+1
-13.65	1.41e+15	3.35e+13	1.00e+15	3.04e+13	4.07e+14	1.94e+13	1.02e+2
-13.41	3.55e+14	1.22e+13	2.44e+14	1.07e+13	1.09e+14	7.17e+12	1.11e+2
-13.17	9.99e+13	4.78e+12	6.13e+13	3.96e+12	3.85e+13	3.14e+12	1.16e+2
-12.93	2.26e+13	1.70e+12	1.20e+13	1.31e+12	1.05e+13	1.23e+12	1.19e+2
-12.69	7.51e+12	7.40e+11	4.09e+12	5.57e+11	3.41e+12	5.08e+11	1.21e+2
-12.46	1.37e+12	2.38e+11	6.41e+11	1.65e+11	7.27e+11	1.76e+11	1.23e+2
-12.22	4.27e+11	1.00e+11	1.89e+11	6.68e+10	2.36e+11	7.47e+10	1.24e+2
-11.74	1.56e+10	1.10e+10	7.45e+09	7.45e+09	7.45e+09	7.45e+09	1.25e+2

^adN/dS has the unit of Deg⁻² (erg cm⁻² s⁻¹)⁻¹.

Table 9. *Swift* Differential AGN Number Counts in the Hard X-ray Band (2–8 keV)

log S (erg cm ⁻² s ⁻¹)	dN/dS						Area (Deg ²)
	<i>Swift</i> -All	uncertainty	<i>Swift-WISE</i> Type I	uncertainty	<i>Swift-WISE</i> Type II	uncertainty ^a	
-14.58	2.26e+17	2.61e+16	1.38e+17	3.07e+16	8.66e+16	2.27e+16	3.020e-1
-14.34	5.37e+16	2.40e+15	3.04e+16	2.60e+15	2.35e+16	2.29e+15	4.669e+0
-14.10	2.03e+16	4.97e+14	1.29e+16	5.22e+14	7.13e+15	3.94e+14	2.218e+1
-13.86	8.05e+15	1.51e+14	5.51e+15	1.55e+14	2.44e+15	1.04e+14	5.119e+1
-13.62	2.53e+15	5.21e+13	1.88e+15	5.20e+13	6.26e+14	3.02e+13	7.481e+1
-13.38	6.29e+14	1.74e+13	4.95e+14	1.69e+13	1.30e+14	8.76e+12	9.322e+1
-13.14	1.53e+14	6.12e+12	1.25e+14	5.96e+12	2.79e+13	2.82e+12	1.047e+2
-12.91	3.83e+13	2.23e+12	3.13e+13	2.15e+12	6.87e+12	1.01e+12	1.123e+2
-12.67	8.32e+12	7.69e+11	6.18e+12	7.09e+11	2.12e+12	4.15e+11	1.174e+2
-12.43	1.99e+12	2.82e+11	1.56e+12	2.71e+11	4.25e+11	1.41e+11	1.204e+2
-12.19	7.28e+11	1.28e+11	4.28e+11	1.07e+11	2.95e+11	8.90e+10	1.220e+2
-11.95	1.03e+11	3.67e+10	5.13e+10	2.56e+10	5.13e+10	2.56e+10	1.231e+2
-11.71	2.96e+10	1.48e+10	2.16e+10	1.25e+10	7.22e+09	7.22e+09	1.242e+2
-11.23	7.32e+09	4.22e+09	4.72e+09	3.34e+09	2.36e+09	2.36e+09	1.252e+2

^a dN/dS has the unit of Deg⁻² (erg cm⁻² s⁻¹)⁻¹.

Table 10. *Swift* Cumulative Cluster Number Counts in the 0.5–2 keV Band

log S (erg cm ⁻² s ⁻¹)	$N(> S)$ (Deg ⁻²)	Area (Deg ²)
-14.36	21.030 ± 1.494	11.36
-14.12	16.904 ± 1.112	23.21
-13.88	9.701 ± 0.625	39.80
-13.65	4.562 ± 0.339	56.07
-13.41	2.037 ± 0.184	71.09
-13.17	1.071 ± 0.122	84.49
-12.93	0.504 ± 0.075	94.75
-12.69	0.258 ± 0.049	103.0
-12.45	0.171 ± 0.039	109.4
-12.21	0.076 ± 0.025	114.4
-11.97	0.050 ± 0.020	118.1
-11.73	0.041 ± 0.018	120.4
-11.49	0.025 ± 0.014	122.2

Table 11. Fitting Results for *Swift* Differential AGN Number Counts

Data Set	Band	Normalization [Deg ⁻² (erg cm ⁻² s ⁻¹) ⁻¹]	Break (10 ⁻¹⁵ erg cm ⁻² s ⁻¹)	a	b
<i>Swift</i> -All	0.5–8 keV	531.91± 250.04	3.67± 1.57	1.34 ^a	2.37± 0.01
<i>Swift-WISE</i> MIR-red	0.5–8 keV	185.08± 13.09	8.10 ^a	1.34 ^a	2.51± 0.02
<i>Swift-WISE</i> MIR-blue	0.5–8 keV	135.34± 10.39	8.10 ^a	1.34 ^a	2.39± 0.02
<i>Swift</i> -All	0.5–2 keV	108.60± 9.78	10.08± 1.40	1.49 ^a	2.54± 0.04
<i>Swift-WISE</i> MIR-red	0.5–2 keV	66.15± 11.80	6.00 ^a	1.49 ^a	2.46± 0.06
<i>Swift-WISE</i> MIR-blue	0.5–2 keV	47.81± 4.73	6.00 ^a	1.49 ^a	2.42± 0.04
<i>Swift</i> -All	2–8 keV	578.61 ^b	2.15 ^b	1.32 ^a	2.39± 0.14
<i>Swift-WISE</i> MIR-red	2–8 keV	168.06± 26.30	6.40 ^a	1.32 ^a	2.46± 0.04
<i>Swift-WISE</i> MIR-blue	2–8 keV	63.95± 12.15	6.40 ^a	1.32 ^a	2.50± 0.06

^aThis parameter is fixed the same as the CDF-S measurement.

^bThe parameters are unconstrained.

Note. — The data are fit by a broken powerlaw with a sharp break as Equation 3.

Table 12. Fitting Results for Cumulative Cluster Number Counts in the 0.5–2 keV Band

Data Set	Normalization (Deg ⁻²)	Break (10 ⁻¹⁵ erg cm ⁻² s ⁻¹)	a	b
<i>Swift</i>	27.73± 2.04	5.10 ^a	0.52 ^a	1.24± 0.04
All	28.13± 0.55	5.10± 1.64	0.52± 0.06	1.22± 0.01

^aThis parameter is fixed as the fitting result using all the data.

Note. — The data are fit by a smooth broken powerlaw as Equation 4 with the smoothness parameter fixed as $c = 2$.